TÉCNICO LISBOA

High-fidelity entanglement generation with imperfect excitations using a single-click scheme

Laura dos Santos Martins

Thesis to obtain the Master of Science Degree in

Engineering Physics

Supervisor(s): Prof. Ronald Hanson
Prof. Pedro José Gonçalves Ribeiro

Examination Committee

Chairperson: Prof. Carlos Manuel Dos Santos Rodrigues da Cruz
Supervisor: Prof. Ronald Hanson
Members of the Committee: Prof. Ernesto Fagundes Galvão
Prof. Gonçalo Nuno Marmelo Foito Figueira
Prof. Pedro Domingos Santos do Sacramento

January 2021

Acknowledgments

First, I would like to thank Sophie for the daily guidance throughout this project. You were always (and I really mean always) available for any question and very dedicated in answering the best way you could, even if it meant looking for and re-checking older notes that were not immediately at hand. I appreciate you making sure I was completely following the discussions and how you were always concerned if was expressing my doubts; I am aware that wasn't always easy. I promise I will continue trying to ask questions. I was particularly surprised how easy and fast it was to get the most detailed feedback from you. I also appreciate how you made sure to not only point things that could be improved, but also to add the positive notes. That gave me a bit more strength to continue towards something better without losing motivation. I am deeply thankful for all your academic and emotional support.

I would also like to thank my supervisor Ronald for welcoming me to be a part of such an exciting research field and giving me the opportunities to grow as a student and as a researcher. I appreciated how you encouraged me to reflect and to formally arrive at the new findings that you were already enthusiastically guessing. The excitement you showed was very rewarding, coming from such an experienced researcher. I also enjoyed your constant good mood and how it made me feel comfortable in a new environment, such a long way from home. I wouldn't be able to be a part of this work without you.

I treasure how Matteo, Simon and Hans were always willing to help and to explain the experimental and conceptual details. You've showed me how great research is based on teamwork and mutual-help. Thank you for making this journey more fun and the working from home less lonely.

A special thanks to Johannes for helping me to go through the dense mathematical calculations and for the fruitful discussions about their interpretation.

An additional thank you note to my co-supervisor, Pedro Ribeiro, for being available to discuss topics outside his range of expertise and for helping me to zoom out and explain my work from another point of view; it was a good practise. I'm also grateful for your help through the formal process.

I want to thank my alphabetically ordered friends, who have been an important part of my life in the last five years - Bia, Bugalho, Dani, Diana, Hector, Ildefonso, João, Marta, Pedro Mendes, Pedro Silva, Rafa and Violeta. Thank you for showing me that my anxieties were also yours and for always being ready to turn our problems into a good laugh. Thank you for the online board games that helped me kill the saudades and clear my mind during lockdown; for working "by my side" on skype, just as if we were studying together; and for keeping me sane during these troubled times. You make me wish these last five years would last forever. Also my long term friends - Ana Rita, Carol, Inês, Mari, Matilde, Mimoso - for turning my mind away from the academic life and helping me balance my life. Thank you João Ferreira and Raphael for always being present and providing me with a sense of security during our time in The Netherlands.

Thank you to my dear boyfriend, Henrique, for all the patience in the world to put up with my ups and downs and for always believing in me, even when I didn't. I thank you for achieving the impossible and actually turning the lockdown into a fun experience, providing me the necessary stability to focus on my work. I appreciate your excitement towards the challenges I was facing and your constant emotional

support.

At last, I'm extremely grateful to my mom, dad and brother for distracting me and putting things into perspective when I needed the most. Thank you for the unconditional support, for never letting me fall and for celebrating my achievements as if they were your own. I appreciate how a simple conversation with you can always put me on the right track when I'm feeling overwhelmed. I owe you everything I've accomplished; Also, a note of gratitude to my grandparents for teaching me there is always a way of seeing the glass half full and that hard work can accomplish great things. You are the most beautiful family.

I've been very lucky for the amazing people that surround me. Thank you all.

Resumo

A caminho da construção de uma rede quântica de grande escala, capaz de assegurar comunicações seguras, diversas experiências de dois nodos foram exploradas. O avanço para uma rede de três nodos exige uma montagem experimental de alto desempenho, capaz de atingir uma elevada fidelidade e taxa de criação de entrelaçamento.

Numa tentativa de mitigar as fontes de erro, investigámos a probabilidade de excitação do centro nitrogen-vacancy (NV), associada ao pulso óptico integrado na sequência de single-click entanglement (SCE). Concluímos que a precisão de calibração da potência do pulso de excitação poderia ser melhorada. Na análise do impacto de um pulso de excitação imperfeito no processo de entrelaçamento entre dois nodos, modelámos a fidelidade de entrelaçamento e a sua taxa de criação em função do ângulo de rotação do pulso óptico, θ. Verificámos que, embora a fidelidade média não seja afectada, a taxa diminui. Adicionalmente se restringirmos a medição de fotões a um determinado detector e fixarmos uma certa diferença de fase óptica, $\Delta\phi$, é possível encontrar estados de alta fidelidade para pequenos valores de θ. As simulações sugerem que a forma mais eficiente de gerar entrelaçamento é encontrando um pulso óptico caracterizado por $\theta = \pi$. Por fim, o modelo desenvolvido foi experimentalmente verificado.

As nossas conclusões deixam em aberto a possibildade de encontrar uma estratégia de entrelaçamento mais eficiente, caso uma investigação futura revele que uma menor potência do pulso de excitação contribui para a diminuição do impacto de outras fontes de erro que foram simplificadas neste projeto.

Palavras-chave: Rede quântica, SCE, angulo de rotação do pulso de excitação, diferença de fase ótica, fidelidade do estado de entrelaçamento, taxa de criação de entreleçamento.

Abstract

On the way to building a large-scale quantum network capable of ensuring safe communications, several two-node experiments have been explored. Stepping up towards establishing a three-node network demands a high-performance setup, able to reach high entanglement fidelity and generation rate.

In a search to mitigate the sources of error, particularly in a nitrogen-vacancy (NV) center based quantum network, we investigated the NV's excitation probability, associated with the optical pulse included in the single-click entanglement (SCE) sequence. We concluded that we weren't perfectly calibrating the excitation pulse power. To assess the impact of a non-perfect excitation pulse on the two-node entanglement process, we modeled the entangled state fidelity and generation rate as a function of the optical pulse rotation angle, θ, that determines the excitation probability. We found that the average fidelity is not affected but the rate decreases. We also observed that if instead of considering the entire system, we restrict the measurement of the heralding photon to a particular detector and set the right optical phase difference, $\Delta\phi$, it is possible to find high fidelity states for small values of θ. The simulations suggest that the most efficient way of generating entanglement is to aim for an optical $\theta = \pi$ pulse. Lastly, we experimentally verified the developed model.

Our findings allow for an increase of the entanglement generation efficiency, as long as future research reveals that a lower excitation power decreases the impact of certain sources of error, whose contributions were simplified in this project.

Keywords: Quantum network, SCE, optical pulse rotation angle, optical phase difference, entangled state fidelity, entanglement generation rate.

Contents

List of Tables

List of Figures

List of Abbreviations

AOM: Acousto-Optic Modulator

APD: Avalanche Photodiode

AWG: Arbitrary Waveform Generator

CR: Charge and Resonance

DD: Dynamical Decoupling

DM: Dichronic Mirror

EOM: Electro-Optic Modulator

ESR: Electro Spin Resonance

MW: Microwave

NMR: Nuclear Magnetic Resonance

NV: Nitrogen Vacancy

PID: Proportional–Integral–Derivative

PSB: Phonon Side Band

RO: Read Out

SCE: Single-Click Entanglement

SIL: Solid Immersion Lens

SP: Spin Pumping

SSRO: Single Shot Read Out

ZPL: Zero Phonon Line

Chapter 1

Introduction

Quantum technologies have become a major research topic, as they promise to offer a radically different approach to computation and communication. In particular, the so called quantum internet has caught the media's attention, mainly by virtue of its intrinsic security [1]. The idea behind it is to build a large scale quantum network that would allow communication of information, in the form of quantum bits or qubits, between any two places on Earth, in a way that any interception of the transmission would be obvious to the user [2]. However, the development of these technologies faces some challenges as the qubits can easily and quickly decohere due to the system's interactions with the environment, making them extremely hard to preserve in time. Therefore, in order to transmit quantum information through large distances, it is not possible to rely on direct transmission of qubits. To overcome this barrier, a quantum network cannot rely on the usual amplifiers to boost the signal during transmission, since the complete state of the qubits would need to be determined and replicated, which is impossible according to the no-cloning theorem [3]. Instead, intermediate nodes, also named quantum repeaters, are necessary to allow communication to be established between distant nodes without physically sending the qubit. The role of a quantum repeater is to, first, intermediate the entanglement pair creation between the two more distant nodes, later allowing a data qubit to be sent using quantum teleportation [2]. Other and more complex uses of quantum communications have been predicted [4] and as the technology is explored, an increasing number of applications arises, fuelling the excitement around this field.

Diverse physical implementations are being studied in the development of the most efficient and reliable quantum network. In this project we use nitrogen vacancy (NV) centers as quantum nodes. The NV centre is a defect in diamond caused by a substitutional nitrogen atom and an adjacent lattice vacancy. It has been proven to be a very promising approach to build the so desired quantum network, mainly due to its good optical interface that promotes spin-photon entanglement [5], long coherence times of the electron spin [6] and the possibility to use the neighboring carbon-13 spins as quantum memories [7]. These advances paved the way to more complex two-node entanglement experiments that have been vastly explored in recent years [8][9] [10], finally leading to the expansion of the quantum network to include an extra node, making it a three node quantum network. Along with the extra node, new exciting experiments on the way and closer to long distance communication mediated by intermediate

nodes, such as three party entanglement and entanglement swapping, become possible. To succeed at these experiments, it is essential to get the best out of all parameters because the sources of infidelity really add up as we increase the number of nodes. It is in this context that this project started, as a way of improving entanglement generated via the single click scheme, such that the three node experiments could succeed. This investigation takes shape with the study of the system's apparent imperfections as tools to maximize the fidelity and rate.

1.1 Thesis Outline

In chapter 2 we introduce all the background necessary to understand this work, starting with the fundamentals of quantum information, continuing with the theory behind NV centers and closing the chapter with the state-of-the-art techniques used to entangle two distant NV centers and to slow down the decoherence of our qubits. In chapter 3, we proceed to present the experimental methods, focusing on the general design of the setups and description of the control mechanisms used to implement the desired parameters. In chapter 4 we begin to study how the optical pulse influences the spin-photon entanglement, in theory, and continue with the experimental verification of the resulting simulations. In chapter 5 we explore the potential consequences of the previous findings regarding the entangled state fidelity and generation rate. This leads to a curious observation that is later analysed and experimentally measured. Finally, chapter 6 closes off the thesis with a summary of the more relevant conclusions and recommendations for future research.

Chapter 2

Theory

2.1 Quantum Information

Quantum technologies rely on the processing, sensing or communication of quantum information, which has quantum bits, also known as qubits, as its basic unit. Qubits are the analogue of bits in classical technologies. There are many different physical implementations of a qubit, but they all consist of a two-level system from which two perfectly distinguishable states of a qubit $|0\rangle$ and $|1\rangle$ emerge. It is possible to mathematically describe a qubit's state as a linear combination, often called superposition, using the state-vector formalism [11]:

$$|\psi\rangle = \alpha\,|0\rangle + \beta\,|1\rangle = \begin{bmatrix} \alpha \\ \beta \end{bmatrix} \tag{2.1}$$

where α and β are two complex numbers that, when taking their modulus squared ($|\alpha|^2$ and $|\beta|^2$), correspond to the probability of measuring the states $|0\rangle$ and $|1\rangle$, respectively. Additionally, it is required that $|\alpha|^2 + |\beta|^2 = 1$, i.e., the sum of the probabilities of measuring each state adds up to 1.

There is an equivalent definition of the qubit's state, up to a global phase, that explicitly incorporates the normalization requirement:

$$|\psi\rangle = \cos\left(\frac{\theta}{2}\right)|0\rangle + e^{i\phi}\sin\left(\frac{\theta}{2}\right)|1\rangle \tag{2.2}$$

where θ and ϕ are real parameters that define a vector within a three-dimensional unit sphere, known as the Bloch sphere (figure 2.1). This allows the perception of the qubit to become more intuitive, given the graphical representation attached.

Density Matrix

An alternate and equivalent formalism for the qubit's description is the density matrix. It provides convenient means for the characterization of a quantum system that is not completely known and it can be written as:

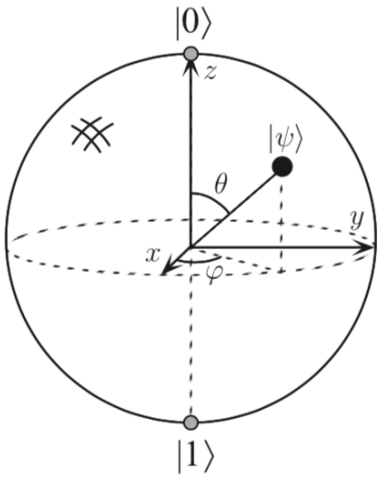

Figure 2.1: Bloch sphere (from [11]).

$$\rho \equiv \sum_i \rho_i \left|\psi_i\right\rangle \left\langle\psi_i\right| \tag{2.3}$$

if it is considered that the quantum system is in one of the i states described as $|\psi_i\rangle$, with respective probability ρ_i. If it is possible to write the density matrix simply as $\rho = |\psi\rangle \langle\psi|$, then ρ is called a pure state, which means the state is completely known. Otherwise, it falls into the category of mixed states, which are not described by the state-vector formalism. The advantage of this representation is that it allows the possibility of describing the lack of information relative to the qubit's quantum state.

Additionally, the density matrix has the following requirements [11]:

- $Tr[\rho] = 1$, all probabilities sum up to 1
- $\rho \succeq 0$, it is semidefinite positive, the eigenvalues are either positive or 0; negative probabilities have no physical meaning

Operations on Qubits

Changes occurring to a quantum state can be described using the language of quantum computation. Analogous to the way a classical computer is built from an electrical circuit containing logic gates, a quantum computer is built from a quantum circuit containing elementary quantum operators to manipulate the quantum information. A quantum operator is a unitary transformation, $\mathcal{U}$, that describes the evolution of a quantum system, in the form:

- $|\psi'\rangle = \mathcal{U}|\psi\rangle$, for the state-vector formalism
- $\rho' = \mathcal{U}\rho\mathcal{U}^\dagger$, for the density matrix formalism

The transformed quantum systems, $|\psi'\rangle$ and ρ', have to fulfill the same requirements as the initial ones, $|\psi\rangle$ and ρ, respectively. A single-qubit operation can also be thought as a rotation in the Bloch sphere. Additionally, quantum operators can further describe stochastic changes to quantum states, characteristic to quantum noise [11], which can be particularly useful in experimental works.

Decoherence

In real-life implementations, quantum systems face a major obstacle as a consequence of their interaction with the environment — decoherence. There are two quantities that characterize this issue. On the one hand, there is the relaxation time, T_1, which describes the energy relaxation of a qubit to its ground state, associated with an absolute loss of information ($|1\rangle$ decaying into $|0\rangle$). On the other hand, the dephasing time, T_2, is related to the deterioration of a pure state to a mixed state. Both phenomena restrain the time associated with the processing and transmission of qubits, but they particularly affect the maximum storage time, essential to the development of a quantum memory. However, generally, T_2 is much smaller than T_1, making T_2 the limiting timescale and object of greatest concern in most quantum experiments.

2.2 The Nitrogen-Vacancy (NV) Center as a Quantum Node

In order to choose from the long list of possible physical implementations of qubits, it is important to identify and prioritize the requirements, taking into account the intentions of the developing technology. In particular, a quantum network node needs to [12]:

- Manipulate quantum states
- Generate entangled states with other nodes
- Store quantum states

The Nitrogen Vacancy (NV) fulfills all the requirements above and is one of the most promising physical implementations. To understand why, it is essential to study its properties and how they can be controlled.

2.2.1 The NV center

An NV center consists of a defect in the diamond lattice caused by a substitutional nitrogen atom and a neighbour lattice vacancy. It has three different types of spin that can be extremely useful: the electron spin, the nitrogen nuclear spin and the surrounding carbon nuclear spin [13].

In the neutral charged state, NV^0, the defect hosts five electrons: three from the bonds of the vacancy's nearest neighbour carbon atoms and two donor electrons from nitrogen. In this project we will focus on the negatively charge state, NV^-, which hosts an extra electron captured from the environment. Figure 2.2 illustrates the six electrons' configuration in the the NV^- orbital ground state. In the excited state, an electron from the a_1 orbital can be excited to one of the two highest energy orbitals, e_x or e_y, because of their degeneracy. The two unpaired electrons, originate a spin singlet and a spin triplet in both the ground and the excited states.

The spin triplet ground state $^3A_2$ is separated from the spin triplet excited states by 1.945 eV (637 nm) (fig. 2.3a). Additionally, the degeneracy between the the levels $m_s = 0$ and $m_s = \pm 1$ spin states is

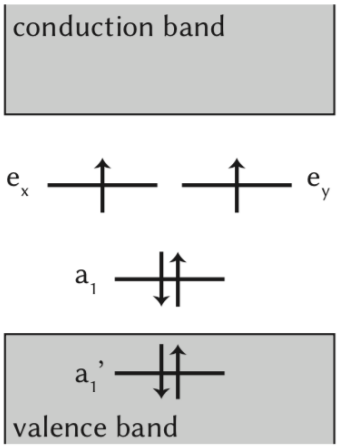

Figure 2.2: Molecular orbitals and their filling in the orbital ground state (from [14]).

lifted, for both the orbital ground state and excited state ($E_{x,y}$ and $E_{1,2}$), due to spin-orbit and spin-spin interactions, originating a zero-field splitting between the two states (fig. 2.3b).

The Hamiltonian of the orbital ground state is:

$$\mathcal{H} = DS_z^2 + \gamma_e \mathbf{B} \cdot \mathbf{S} \tag{2.4}$$

where the zero-field splitting is $D \approx 2.88$ GHz and S_i are the Pauli spin operators. The presence of a magnetic field, B, along the NV axis, lifts the degeneracy from the $m_s = \pm 1$ states through the Zeeman effect and gyromagnetic ratio $\gamma_e = 2\pi \cdot 2.802$ MHz/T [15] (fig. 2.3c).

The degeneracy between the $E_{x,y}$ and $E_{1,2}$ states can be lifted by a lateral strain or an external electric field.

The NV can be excited by both resonant or non-resonant light. In the later case, the NV is excited to a level in the phonon-side band (PSB), rapidly decaying to ${}^3E$ by emitting a phonon. The excited state can decay directly in the ${}^3A_2$ state, emitting a photon in the zero-phonon line (ZPL) or it can decay to the PSB of the ground state, emitting a less energetic photon. About 3% of the photons are emitted in the ZPL and the rest is in the PSB. However, the transition between the excited to the ground state can also occur via the singlet states that lay in between the triplet states, providing a way of non-radiative decay.

2.2.2 Electron spin as central qubit

Since it is possible to discriminate $m_s = 0$, $m_s = -1$ and $m_s = +1$ energies of the orbital ground state, it is also possible to individually address the electron transitions to and from $m_s = 0$, through microwaves with frequencies resonant with the desired transitions. This means the two-level system that defines the qubit's computational basis can be defined as $m_s = 0 := |0\rangle$ and $m_s = -1 := |1\rangle$.

Once the qubit is defined, and in order to fulfil all the quantum network's requirements mentioned above, it is necessary to learn how to initialize, manipulate and measure the system.

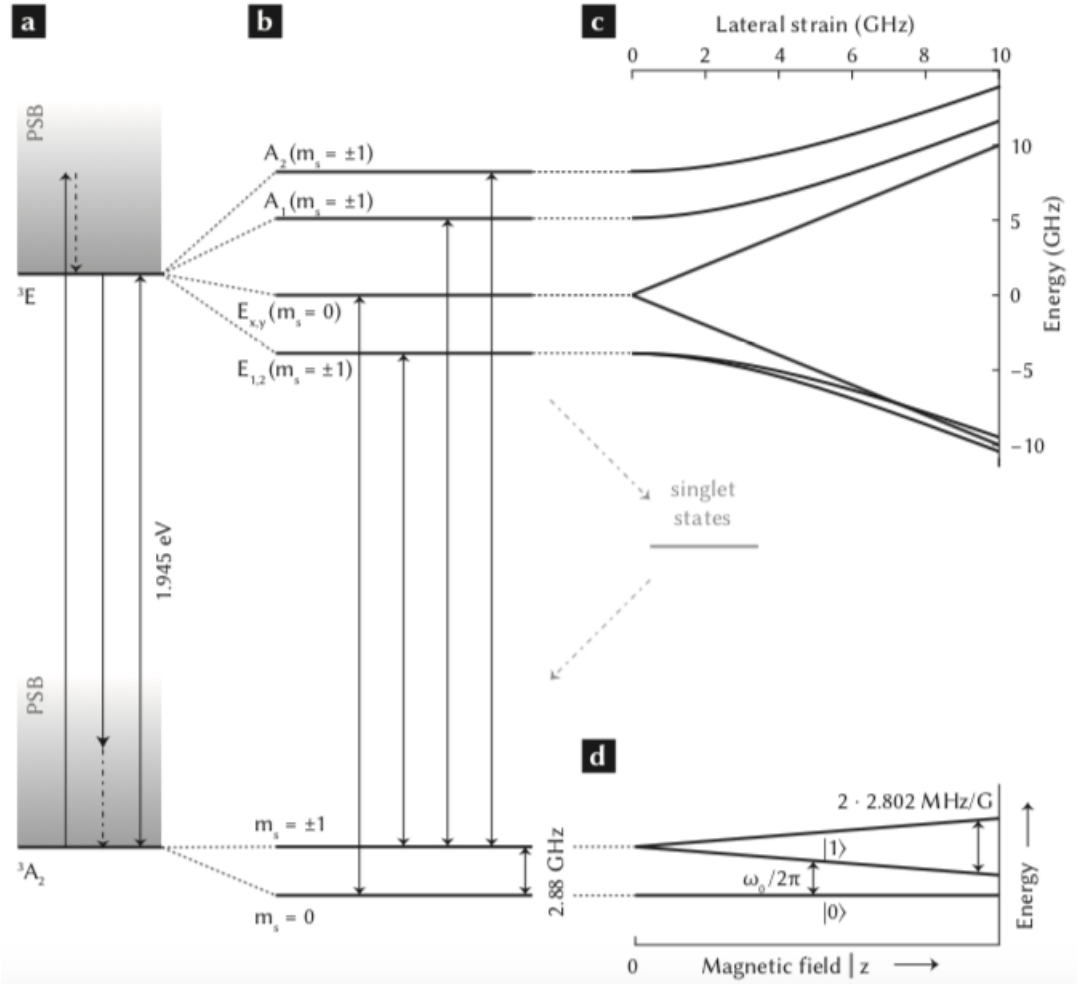

Figure 2.3: Electronic structure of NV^- (from [14]).

Initialization and read out

Before any protocol can be implemented, there is the need to ensure the qubits are in the desired initial states and that they can be measured, in order to verify if the experiment was successful.

As it has been already seen, at cryogenic temperatures, there is a discrete energy spectrum that allows us to selectively address the desired transitions. Therefore, both the preparation and readout techniques can rely on the resonant excitation of spin-selective optical transitions. In particular, both E_x and A_1 transitions are particularly useful: A_1 connects the ground and excited states with spin projection $m_s = \pm 1$, whereas E_x connects states with $m_s = 0$ spin projection [14], as shown in figure 2.4(a).

Upon optical excitation, resonant with E_x or A_1 (Fig. 2.4(a)), the NV^- will later decay back to its orbital ground state, after an optical lifetime of 12 ns [5]. Due to a slight spin mixing (mostly suppressed by low temperatures) within the excited states and to the decay via the singlet state, there is a small probability that the spin is flipped upon returning to a lower energy level. This can be seen in the fluorescence's decay over time, under resonant excitation (figure 2.4(b)). This optical pumping mechanism enables high-fidelity spin state initialization [5]. In general, we initialize the electron spin in the $|0\rangle$ state via spin pumping, using the A_1 transition and initialize in $|1\rangle$ state with an additional MW pulse.

Spin-dependent resonant excitation also allows single-shot electronic spin readout, since the pres-

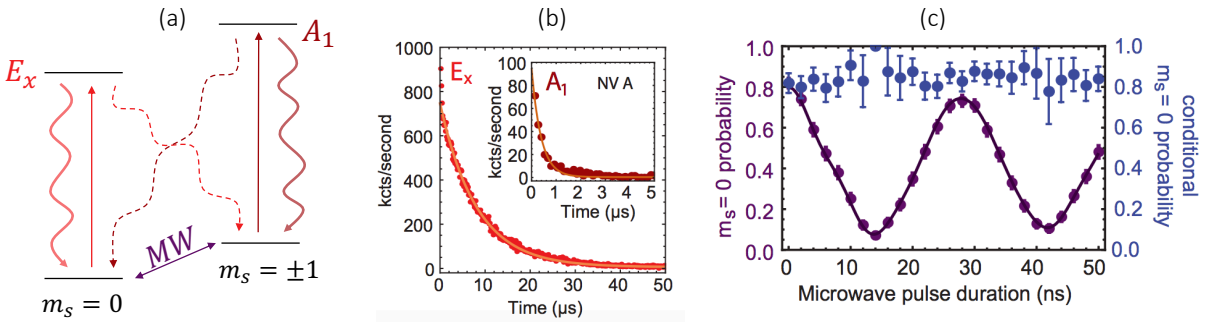

Figure 2.4: Initialization and Control (from [5]). (a) Relevant optical transitions of the NV. (b) Exponential decay of the fluorescence with time under optical excitation. (c) Microwave control of the NV's quantum state (purple); Measurement outcome after projection into $m_s = 0$ (blue).

ence or absence of fluorescence under resonant E_x excitation reveals the spin state. More specifically, if the spin is initialized into $m_s = 0$, photons will be detected as opposed to a $m_s = -1$ spin projection initialization.

Control

Microwaves pulses can be used to control the qubit's state through Rabi oscillations[1], as it is illustrated in figure 2.4(c) (purple). Depending on the duration of the microwave pulse, the projected spin varies coherently between the states $|0\rangle$ and $|1\rangle$, passing through superpositions in between [5]. An important note is that, if after the first measurement, in which the spin is measured to be in the $|0\rangle$ state, the same electron spin is measured for a second time, it is obtained a high probability to measure the spin in the state $|0\rangle$, independently of the microwave pulse duration before the first measurement (Fig. 2.4(c) (blue data)). This means that, as expected, the measurements are projective.

2.2.3 Entanglement generation

A key aspect that allows taking full advantage of the system's quantum properties and unique advantages is entanglement, e.g. because it permits the determination of the entangled system as a whole by simply measuring one of its particles. For an NV center, it is particularly simple to generate entanglement by taking advantage of the electron spin-photon interaction. More specifically, it is possible to emit a photon under the condition that the electron spin state is $|0\rangle$, if a pulse resonant with E_x is applied. Mathematically, the resulting state is written as[2] $|NV, photon\rangle = \frac{1}{\sqrt{2}}(|01\rangle + e^{i\phi}|10\rangle)$, which corresponds to a maximally entangled state up to a local phase, ϕ. Different optical techniques allow further entanglement of two distant photon emitters (see section 2.3.1) [17–19].

[1] Rabi oscillation is the cyclic behaviour of a two-level quantum system in the presence of an oscillatory driving field. The quantum operation parameters are defined by the phase and frequency of the driving wave [16].

[2] The second qubit corresponds to the presence, $|1\rangle$, or absence, $|0\rangle$, of a photon.

2.2.4 Nuclear Spins as Quantum Registers

It is essential that quantum networks are also able to store information, since memory qubits allow for multi-node protocols that rely on multipartite entangled states. Therefore, there is the need for quantum nodes to preserve the state of the qubit for a long time. As mentioned before, decoherence might be an obstacle, which is why long coherence times are such an attractive feature for quantum networks.

Nuclear spins in solids are promising candidates for quantum registers because of their long coherence times [20] and availability of well-established nuclear magnetic resonance (NMR) techniques to manipulate them [21]. In particular, nuclear spins in diamond that couple weakly to the electronic spin of an NV center have shown great potential in quantum registers in several experiments in recent years [22, 23].

2.2.5 Advantages of using NV centers in quantum networks

The NV is a great candidate for a quantum node — and the one chosen in QuTech's implementation — in part because of its long coherence times[3], even at room temperature. Additionally, the combination of different qubits (electron spin, nuclear nitrogen spin and carbon nuclear spin) facilitates the storage and processing of quantum information. Finally, the electron spin also interacts with photons, which allows the transmission of quantum states and the connection and entanglement of NV centers, over long distances.

2.3 State of the Art

Quantum channels enable the implementation of communication tasks, inaccessible to their classical counterparts. The most famous example is the distribution of secret key. However, in the absence of quantum repeaters, the rate at which these tasks can be performed is dictated by the losses in the quantum channel. Moving beyond two-node networks, might significantly increase the secret-key rate and reach beyond the limits of direct transmission. However, no experimental implementation has overcome the direct transmission threshold, mainly due to the poor entanglement-generation rate. Motivated to overcome this barrier, the authors in [24] propose a set up based on nitrogen-vacancy (NV) centers in diamond, embedded in an optical cavity to improve the probability of successfully detecting an emitted photon, combined with a Single-Click Entanglement (SCE) scheme. They predict that, in these conditions, it will be possible to surpass the capacity of the highest secret-key rate, achievable with direct transmission, by a factor of 7 and for a distance of approximately 9.2 km.

2.3.1 Single-Click Entanglement (SCE)

Entanglement between two nodes can be generated in different ways. The majority of previous works on NV centers have used techniques that rely on the detection of two photons [9]. However, a different

[3] the diamond lattice consists to 98.9% of spinless ^{12}C, leading to only slow dephasing from a fluctuating nuclear spin bath.

technique, which relies on the detection of a single photon, more specifically the Single-Click Entanglement (SCE) [8], will be used in this work. This protocol starts by initializing two distant NV centers (NV_1 and NV_2) in the same state:

$$|NV\rangle_i = \sqrt{\alpha}\,|0\rangle_i + \sqrt{1-\alpha}\,|1\rangle_i \quad , \qquad \text{i=1,2.} \tag{2.5}$$

The emission of photons can be conditioned by the state of the qubit if optical pulses, resonant with a particular transition (E_x in this case), are applied. In other words, it is possible to entangle the $|0\rangle$ ($|1\rangle$) state of each NV center with the presence (absence) of a photon, which is mathematically translated to:

$$|NV, photon\rangle_i = \sqrt{\alpha}\,|01\rangle_i + \sqrt{1-\alpha}\,|10\rangle_i \quad , \qquad \text{i=1,2.} \tag{2.6}$$

The photons emitted by each NV are then transmitted to a beamsplitter, to remove the which-path information. Upon the detection of a single photon, it is revealed that one of the NV's was in the $|0\rangle$ state (it was optically excited and emitted a photon) while the other was in the $|1\rangle$ state (remained unchanged). In other words, the NV's state is ideally projected onto the maximally-entangled Bell state: $|\psi\rangle = |NV_1, NV_2\rangle = \frac{1}{\sqrt{2}}(|01\rangle + |10\rangle)$. Nonetheless, taking into account the small photon detection efficiency ($p_{det} \ll 1$), the non-number resolving detectors and the optical phase acquired by the laser pulses, used to create spin-photon entanglement, as well as the optical phase acquired by the emitted photons as they propagate (total optical phase difference of $\Delta\phi$) [8], the generated state degrades to:

$$\rho_{NV_1,NV_2} = (1-\alpha)\left|\psi^{\pm}\right\rangle\left\langle\psi^{\pm}\right| + \alpha\,|00\rangle\langle 00| \tag{2.7}$$

with

$$\left|\psi^{\pm}\right\rangle = |NV_1, NV_2\rangle = |01\rangle \pm e^{i\Delta\phi}\,|10\rangle\,, \tag{2.8}$$

where the $\pm$ depends on which detector clicks. In order to ensure that the entangled states generated are available for further use, we need to know exactly what states are being generated, which requires this optical phase difference $\Delta\phi$ to be known. The measurement and stabilization of this parameter is described in section 3.3. The theoretical fidelity[4] of this state with the maximally entangled state is $\mathcal{F} = 1-\alpha$ and the probability of successfully heralding entanglement is given by $2p_{det}\alpha$. Thus, it is necessary to adjust the value of α, in order to obtain the desired entanglement rate, without compromising too much the associated fidelity.

2.3.2 Slowing down decoherence

The electron spin in each NV center is surrounded by a cloud of nuclear spins. Around 1% of the diamond is composed by ^{13}C, which is a spin-half system, and the rest consists of ^{12}C, which has no spin. These nuclear spins are a source of decoherence as they flip flop randomly, creating a slow variation of the magnetic field that surrounds the electron spin. This fluctuations change the energy

[4]The fidelity of a quantum state is a measure of the "similarity" of two quantum states, ρ and $|\sigma\rangle$ (a pure state in this case), defined as $\mathcal{F} = \langle\sigma|\,\rho\,|\sigma\rangle$.

levels of the NV center, which causes the phase evolution of a quantum superposition state to become random, causing the loss of its quantum properties.

In order to slow down decoherence, it is possible to apply a dynamical decoupling sequence as showed in figure 2.5.

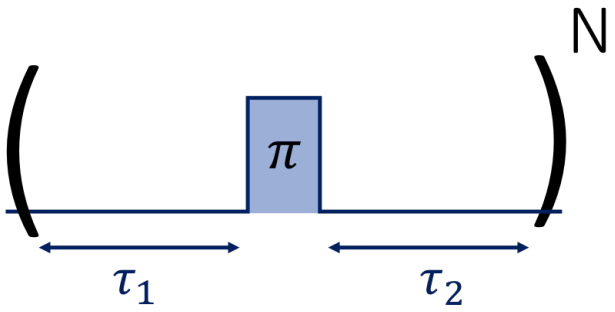

Figure 2.5: Simplified dynamical decoupling sequence. τ_1 corresponds to the dephasing time between the qubit's initialization and the phase flip resulting from the π pulse, while τ_2 corresponds to the dephasing time between that same phase flip and the end of the sequence, where we should recover the initial state. The ideal number of repetitions of this sequence, N, depends on the fluctuations of the surrounding magnetic field.

In a graphical way, the dephasing can be explained by imagining a $|+\rangle$ state, in the Bloch sphere, that rotates on the xy plane, as a consequence of the magnetic field, B_z. As this magnetic field changes randomly, the rotation around the z axis varies accordingly, which means the phase evolution is randomized and the qubit's quantum state is lost. As a solution, we let the system, initialized in $|+\rangle$, evolve during a time, τ_1. It follows a π rotation around the y axis that flips the qubit and inverts the effect of the magnetic field on the electron spin. In the end it is only necessary to let the qubit evolve for another time interval, τ_2 until it goes back to the original $|+\rangle$ state. There are two requirements for the effect of the magnetic field to be exactly canceled, successfully preserving the quantum state:

- The time before and after the flip has to be the same ($\tau_1 = \tau_2 = \tau$).
- Either the magnetic filed is constant over time, τ, or the qubit is flipped multiple times, N, so that the changes in the slow varying magnetic field average out. In other words, τ needs to be much smaller than the timescale of the changes in the magnetic field.

The method that was just described corresponds to the simplest approach that serves as a principle for other more complex solutions to the decoherence problem, namely the DD protocols with two-axis control, i.e., with alternating phases of the π pulses, as a way to protect the qubit from pulse errors [25]. This technique is able to protect a qubit for over a second [26], which is 6 orders of magnitude better than without any correction.

2.3.3 Quantum Memory

Realizing larger multi-qubit registers is challenging due to the need for quantum gates that avoid crosstalk and protect the coherence of the complete register. In [27], the authors present novel decoherence-

protected gates that combine dynamical decoupling (DD) of an electron spin with selective phase-controlled driving of nuclear spins. They realize a 10-qubit quantum register consisting of the electron spin of a nitrogen-vacancy center and 9 nuclear spins in diamond. The register was fully connected, as entanglement between all possible 45 qubit pairs is successfully generated. Coherence times are the longest reported for a single solid-state qubit, reaching up to 63 seconds. Finally, they store two-qubit entangled states for over 10 seconds, which is 6 orders of magnitude better than without any correction. These results open the door to advanced quantum algorithms and quantum networks with NV center qubits.

2.3.4 Initialization and Read Out Fidelity

In order to have successful experiments, it is important to ensure that the state, in which the system is initialized, is known and that the measurement results correspond to the actual state of the qubit. This generally reflects into high fidelities and small errors. Recent experiments, using NV centers, have achieved a combined initialization and single-shot read-out fidelity of $(97.1 \pm 0.2)\%$ [9].

Chapter 3

Experimental methods

3.1 Samples

An NV center consists on a defect in the diamond lattice caused by a substitutional nitrogen atom and a neighbour lattice vacancy. The NV centers used in this experiment naturally occur in chemical vapor deposition grown ultra-pure type IIa diamonds, supplied by Element Six. In order to improve the photon collection efficiency, solid immersion lens (SIL) are fabricated around the NV's (see fig. 3.1), minimizing the internal reflection and an Al2O3 anti-reflection coating is deposited on top of the diamond, improving the signal-to-noise ratio. On the surface of the diamond, next to the SIL's, are a gold strip line for applying magnetic resonance pulses (radio and microwave) and gold electrodes for applying DC voltages, that shift the optical resonances of the NV centre by the DC Stark effect, allowing two separate NV centres to emit indistinguishable photons, and thereby opening doors for remote entanglement.

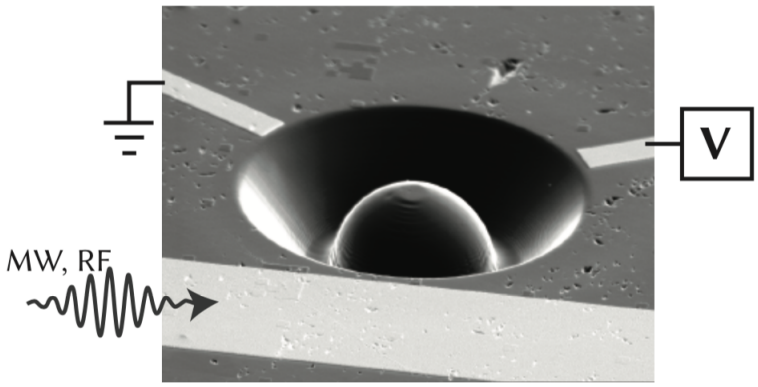

Figure 3.1: The NV sample (from [14]).

3.2 Setups

The excitation light is focused onto the NV through a microscope objective located above the cryostat. The same objective collects the emitted photons. Additionally, a half wave plate is placed right before

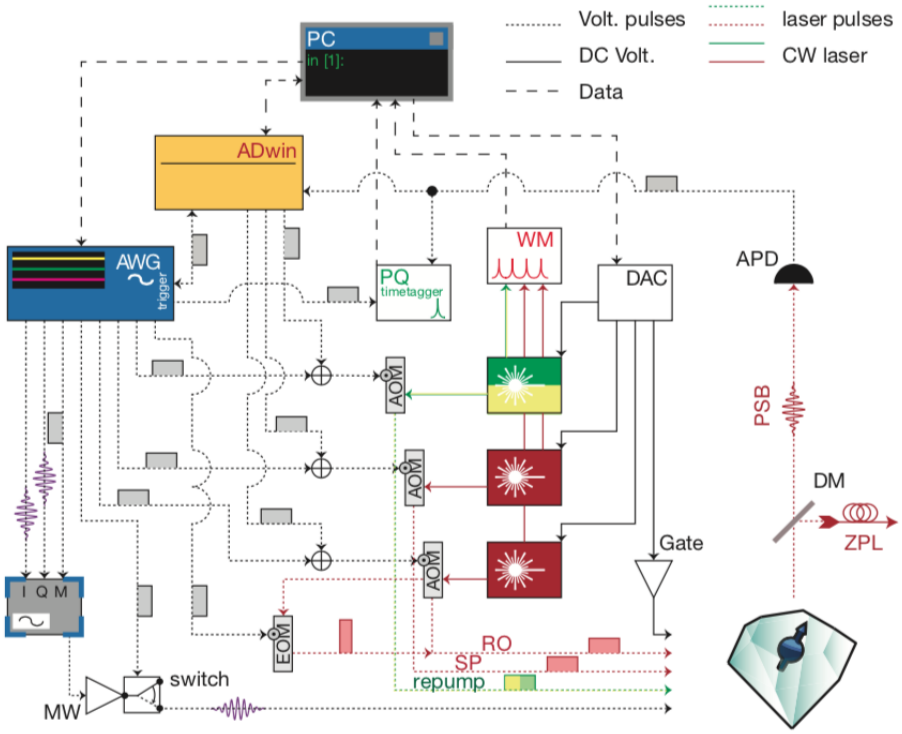

Figure 3.2: Single-setup control (from [14]). A PC programs the control loop on a microcontroller (ADwin) and pulse sequences on an arbitrary waveform generator (AWG). The ADwin triggers the AWG to start the pulse sequences and the AWG notifies the ADwin when they are completed. The lasers pulses for charge re-pumping (Green/Yellow), electron spin pumping (SP) and electron spin read-out (RO) are generated via acoustic-optic modulators (AOM's), controlled by both the AWG and ADwin. In addition, the RO laser pulses can be modulated into nanosecond optical excitation pulses via an electro-optic modulator (EOM), controlled by the AWG. The laser frequencies are read by a wavemeter and adjusted by a proportional–integral–derivative (PID) controller on the PC. The frequency adjustment signal from the PC is fed into a digital to analog converter (DAC) that is connected to the lasers. The microwave (MW) source, controlled by the AWG, outputs a signal that is later on amplified and put through a MW switch, also controlled by the AWG, to reduce the noise. Additionally, the gate voltage is controlled by a PID controller on the PC.

the objective (cryo half wave plate), such that we can control the polarization of the excitation light (see appendix A.1.11).

The zero-phonon line (ZPL) and phonon side band (PSB) photons, emitted by the NV upon excitation, are split into different paths by a dichroic mirror (DM). The PSB photons are then detected by an avalanche photodiode (APD). The ZPL photons are further filtered by another DM to separate them from the green excitation light. Resonant excitation light is then filtered by a half and a quarter wave plates and a polarizer and then detected by a superconducting nanowire single-photon detector. The APD's are connected to the ADwin and to a time-to-digital converter (PQ time-tagger) for counting and synchronization purposes, respectively.

3.2.1 CR Check - Charge state verification and resonance check

Resonant excitation light can ionize the NV^- defect and turn it into the undesired neutral charge state. Additionally, the local charge environment of the defect can fluctuate, changing the the optical transition

frequencies. These changes may induce different set ups to emit photons with different frequencies, breaking the indistinguishably condition, required to generate remote entanglement. Therefore, a sequence for charge state verification and resonance check was developed [28]. Before the experiment starts, the verification step starts by simultaneously turning on the spin pump and the read-out lasers, while the fluorescence is detected. Given that the laser frequencies are set to be resonant with the optical transitions of the NV^- charge state and that these same frequencies are no longer resonant with the optical transitions of the NV^0 state, it is expected that the number of counts is significantly lower for the last case. Therefore, it is necessary to set the minimum number of counts that characterizes the negative charge state, thr_1. In case the number of counts is smaller than the defined threshold, the green/yellow laser is turned on, such that the NV^- charge state is recovered, followed by another verification step. However, this repumping process can change the local charge environment, therefore changing the resonance frequencies. Consequently, after the first threshold is exceeded, the minimum number of counts that is to be accepted for the experiment to continue, thr_2, is set such that if the number of counts is larger than the threshold, the experiment can continue, otherwise we change the gate voltage such that we bring the NV back to an on-resonance configuration. Finally, an extra threshold can be set such that if the previous CR check was successful, the number of counts necessary to continue the experiment is thr_3. All thresholds are determined by hand, based on CR check statistics.

3.3 Phase stabilization

The entangled state prepared using the single click scheme (see section 2.3.1), in an ideal system with no losses, that relies on perfect detectors able to resolve the number of photons that reach them, is described by equation 2.8. Assuming the target state, i.e., the final state we intend to generate, is $|\psi\rangle = \frac{1}{\sqrt{2}}(|01\rangle + |10\rangle)$, the fidelity of the entangled state prepared in this ideal system can be written as

$$\mathcal{F}(\Delta\phi) = \frac{1}{2} + \frac{1}{2}\cos\Delta\phi. \tag{3.1}$$

In order to experimentally demonstrate that we are able to generate entanglement, we need to prepare and measure several entangled states. If this optical phase difference, $\Delta\phi$, resulting from the path length difference that the photons travel through before interfering at the beam splitter (see section 2.3.1), changes during experiments, then the heralded states are no longer consistent, which is mathematically equivalent to integrating the effective entangled state over all possible phases, arriving at a fidelity of 0.5, which corresponds to the threshold at which an entangled state becomes unusable. In the particular experimental apparatus used throughout this project, the two main sources of noise, responsible for the optical phase difference fluctuations, have been identified to be the vibrations of the optical fibers and the vibrations induced by the cryostats, used to keep the samples at low temperatures, onto the sample stages or microscope objectives. In order to mitigate this source of infidelity, we stabilize the optical phase difference to a pre-determined set point before the heralding click, making sure we are consistently preparing the same entangled state and that we know exactly what that state is. As a

consequence, this phase will be characterised by a Gaussian distribution whose standard deviation, σ, corresponds to the phase uncertainty, $\delta\phi$, culminating in a fidelity given by

$$\mathcal{F}(\delta\phi) = \frac{1}{2} + \frac{1}{2}e^{-(\delta\phi)^2/2}. \tag{3.2}$$

If we want to arrive at the fidelity expressed in equation 3.2, we need to be able to actually stabilize this phase, $\Delta\phi$. To do that, a combination of homodyne and heterodyne phase detection is used. Unlike the homodyne phase detection scheme that, as the name suggests, requires the light in both arms of the interferometer to have the same frequency, the heterodyne phase detection scheme actually relies on distinct frequencies for each arm. Consequently, the intensity in the output ports, $I_{3,4}$, will naturally depend on which phase detection scheme we are using. More specifically, considering the input light intensities, $I_{1,2}$, and frequencies, $\omega_{1,2}$, and assuming the light is linearly polarized and perfectly overlapping spatial modes [29], the output intensities may be described by constructive or destructive interference, depending on $\Delta\phi$ (equation 3.3) for homodyne phase detection or result in a beat signal (equation 3.4) for heterodyne phase detection.

$$I_{3,4}^{homodyne} = I_1 + I_2 \pm 2\sqrt{I_1 I_2}\cos\Delta\phi \tag{3.3}$$

$$I_{3,4}^{heterodyne} = I_1 + I_2 \pm 2\sqrt{I_1 I_2}(\cos\left((\omega_1 - \omega_2)t - \Delta\phi\right) + \cos\left((\omega_1 + \omega_2)t - \Delta\phi\right)) \tag{3.4}$$

Equation 3.4 shows that the amplitude of the beat signal, in the case of the homodyne phase detection, does not depend on the phase, which means that the phase measurement is not vulnerable to fluctuations of the input light, on the contrary to what happens when we rely on homodyne phase detection. Additionally, it shows we can control the amplitude of the beat signal just by increasing the input intensity of one of the arms, which facilitates the measurement of small signals. However, the phase detection scheme we use for each interferometer depends on the requirements of each part of the set up.

3.3.1 Implementation

In a three-node experiment, there are two interferometers that need to be stabilized, one for the first (A-B) and the other for the second (B-C) spin-spin entanglement. The two entanglement pairs have one node in common, node B. Therefore, both interferometers share part of their optical paths, more specifically, the path used for exciting the NV and collecting the resulting photons from node B, conducting them to the detectors after passing through the beam splitter.

In order to stabilize the phase to a given set point before entanglement is attempted, the optical phase difference needs to be measured before an adjustment to the optical pathlength can be made. The phase difference measurement relies on classical interference of excitation light reflected off the diamond surface. However, this signal is minimized such that we can distinguish reflected excitation light from the ZPL photons that will herald entanglement (see section A.1.11). Therefore, this signal is very small, demanding a long time for phase stabilization. To avoid this, the two interferometers are split

into six different interferometers [30] and a different light source (purple lines in figure 3.3) is used to stabilize the path that otherwise would have a very small signal, ensuring all the interferometers have enough light to stabilise relatively fast, while maintaining an optimal rejection of the excitation light.

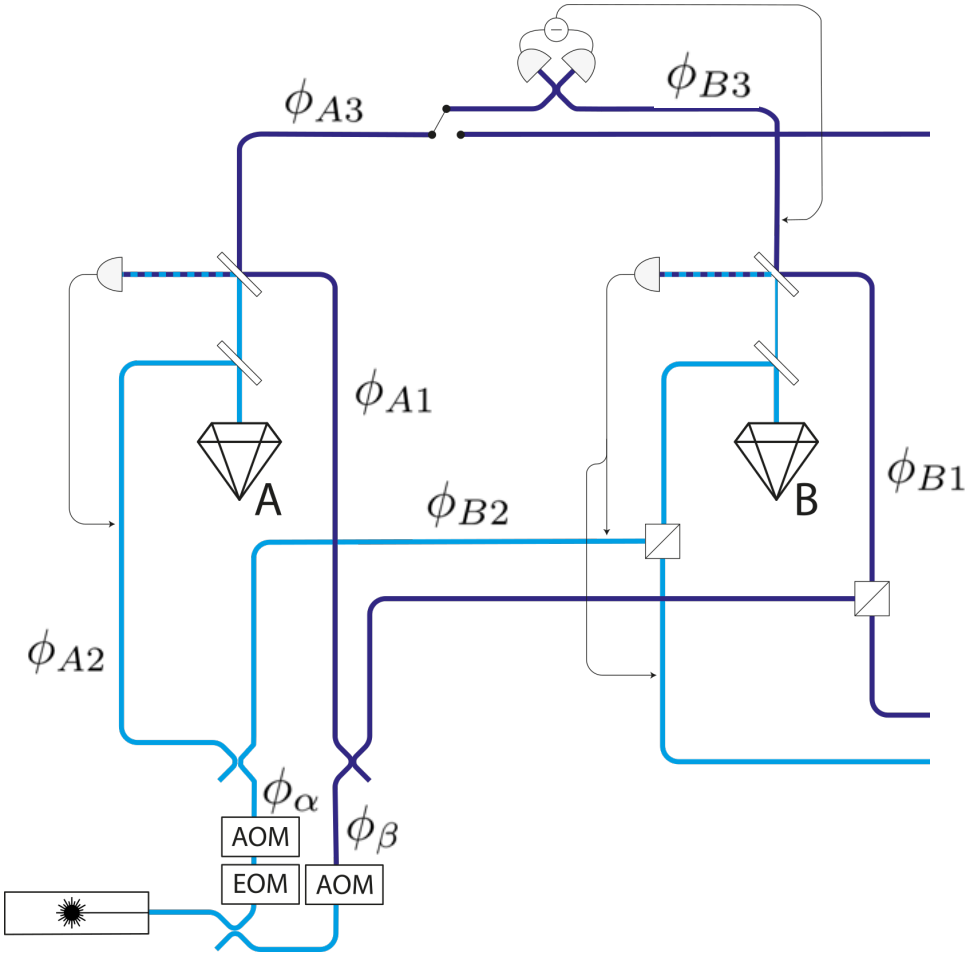

Figure 3.3: Phase stabilization scheme (adapted from [30]). Three out of six interferometers are represented. The cutted lines lead to node C, which operates with node B analogously to what is depicted in this figure. The excitation laser, concerning the solid blue lines, has the same frequency as the $|0\rangle \leftrightarrow |e\rangle$ transition, whereas the phase light, concerning the solid purple lines, has a frequency offset of 10 MHz with regards to the excitation laser. Locally, the heterodyne beat signal (intermittent blue and purple line) is measured and compared to an electronic reference signal. Globally, the interference is measured by the single photon detectors. An optical switch allows the same single photon detectors to be used for both entanglement pairs. After the phase measurement, feedback to the optical paths is applied to a fiber stretcher, in the case of global phase stabilization, and on a mirror on a piezoelectric element, in the case of local phase stabilization.

Figure 3.3 illustrates a diagram of three out of the six combined interferometers, where each optical path is associated with a phase, ϕ_i, that corresponds to the phase that an electromagnetic wave going through that same path would acquire. Although the used setup consists on a three-node network, in order to avoid redundancy, the diagram illustration and associated equations, presented in this section, exclusively regard a two-node phase stabilization. The reason for this being that the exact same representations apply to the third node, i.e., if node B and all its associated $\phi_{Bi,\beta}$ are fixed, then writing node A or C is simply a matter of labelling, since their surrounding setups are analogous and the same conditions apply. Therefore, we can consider that for every equation presented in this section, the same

is required for the third omitted node.

The condition we want to enforce to guarantee phase stability for A-B entanglement is equation 3.5 for phase stab first.

$$\phi_{A2} + \phi_{A3} - (\phi_{B2} + \phi_{B3}) = W \tag{3.5}$$

W takes different values, depending on the desired entangled state phase, $\Delta\phi$ [1]. However, this interferometer was split into three different ones, which naturally implies three different conditions we need to verify for each entanglement link, described by the following equation system

$$\begin{cases} \phi_{A1} + \phi_{\beta 1} - (\phi_{A2} + \phi_{\alpha}) = X \\ \phi_{BA1} + \phi_{\beta 1} - (\phi_{BA2} + \phi_{\alpha}) = Y \\ \phi_{A1} + \phi_{A3} - (\phi_{BA1} + \phi_{B3}) = Z \end{cases} \tag{3.6}$$

where $Z - X + Y = W$. It is worth mentioning that the phase measurement only determines the phase within $180°$, i.e., from $-90°$ to $+90°$. Once this phase is measured, the setup is adjusted such that the phase is set to its pre-determined value, W. Logically, the closer the measured phase is to the set-point, the smaller the modification of the setup and the more stable the system is, making the $0°$ set-point the logical choice, if no specific $\Delta\phi$ is required. However, if that is not the case and we intend to stabilize the interferometer at $W = +90°$, we would have a lot of phase measurements away from that point, which would hamper the stabilization and result in a larger uncertainty, since the system would be subject to bigger changes. Luckily, with the fragmentation of the interferometer, we can easily choose any entangled state phase, $\Delta\phi$, with no restrictions, since it allows us to play with three different set-points instead of one, therefore making three small changes (X, Y and Z) instead of a single abrupt one (W), not jeopardizing the stability of the setup.

The global interferometer, concerning the last condition in equation system 3.6, stabilizes the optical path connecting the nodes to the central beam splitter, via single-mode optical fibers. Due to the limited bandwidth of the single photon detectors and considering the fact that entanglement generation requires the arms to have the same frequency, homodyne phase detection is used for the global interferometers. The interference signal is measured by the same single photon detectors used for the heralding click and the optical phase difference is calculated using the intensity difference measured between the two detectors. Since these two detectors are shared for both entanglement links, the same switch we use to select which two nodes we want to use for experiment, is used to select the interferometer we want to stabilize, i.e., link A-B or B-C.

Locally the optical paths are stabilized using heterodyne phase detection, given that this method is not sensitive to intensity fluctuations and there are no setup conditions preventing us from choosing it. This part of the interferometer is responsible for the stabilization of the excitation path and free space optical path close to the cryostat, which is achieved by means of enforcing the first and second conditions

[1] The purpose of this section is to show how the phase can be stabilized to a given set-point, how to further determine W as a function of $\Delta\phi$, will become clear in the next chapter.

in equation system 3.6. The beat signal (intermittent blue and purple line in figure 3.3) is produced by combining the reflected excitation pulse in arm, that can be separated from the photons emitted by the NV using a polarizing beam splitter (PBS) (see section A.1.11), with a strong laser pulse with a frequency offset of 10 MHz (solid purple line in figure 3.3) in the other arm. The beat signal is measured by a photodiode detector and the optical phase difference is extracted by comparing this signal with a reference wave. The middle node (B) can be excited by two different lasers, depending on what other node (A or C) we intend to use for entanglement, which means that two local paths associated with this node can be stabilized, leading to two different local interferometers.

Finally, the measured phase is used to compute the feedback that needs to be applied to the optical path with a mirror on a piezoelectric element, in the case of local phase stabilization, or a fiber stretcher, in the case of global phase stabilization.

Once all interferometers are stabilized, we can be sure we are always preparing the same entangled state, whose fidelity, written as a function of the desired optical phase difference, $\Delta\phi$, is described by equation 3.2.

Chapter 4

The effect of the optical excitation pulse on spin-photon entanglement

Taking into consideration that three-node experiments usually rely on multi-qubit entangled states, the entanglement generation rate and the fidelity of the prepared entangled states are critical for the success of the experiments.

In order to make sure we minimize every source of infidelity, we first need to identify them and then find out if there is some way we can correct for them.

Every attempt of generating entanglement between two nodes starts with the entanglement of the electron spin state and a photon state, for each set up, obtained through the sequence depicted in figure 4.1.

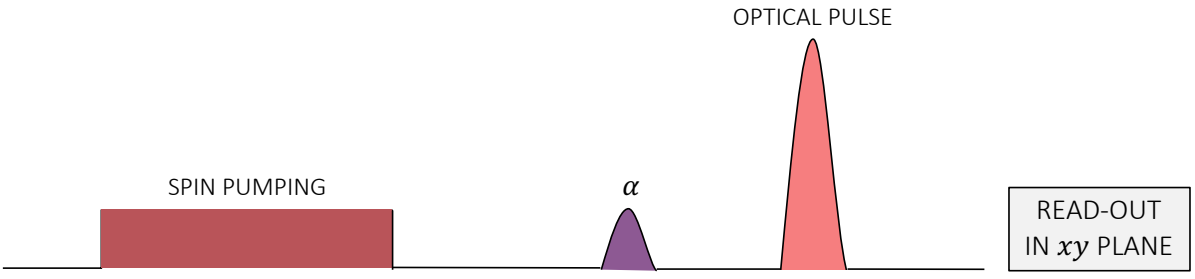

Figure 4.1: Spin-photon entanglement test sequence. It starts by spin pumping (SP) the electron spin in the $|0\rangle$ state, bringing it to a superposition with a MW α pulse and a 2ns optical π pulse that excites the population in the $|0\rangle$ to the $|e\rangle$ state. Upon decay, the electron spin will be entangled with the photon state. Finally, the NV is measured in the xy plane of the Bloch sphere.

The spin-spin entanglement is mediated by the spin-photon entanglement of each node. Therefore, it is necessary to verify if the spin-photon entanglement sequence, in each node, produces the expected results.

To test this, we consider the case where an entanglement attempt is performed but the photon is not measured, i.e., we initialize the electron spin state, bring it to a superposition state ($\sqrt{\alpha}\,|0\rangle + \sqrt{1-\alpha}\,|1\rangle$) and send an optical excitation pulse such that the density matrix that describes the spin-

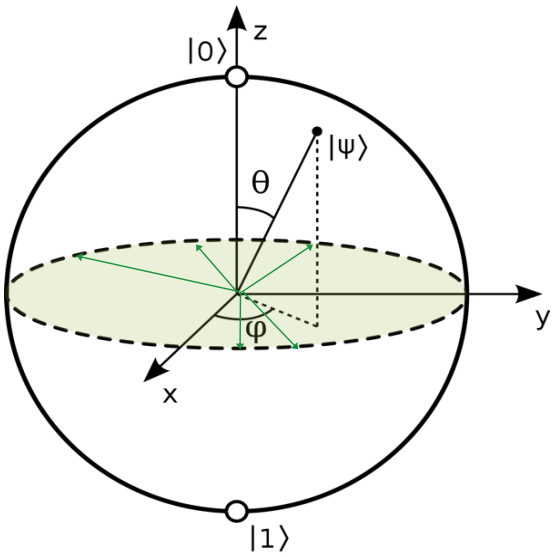

Figure 4.2: Bloch sphere representation of the xy plane measurement axis. The green plane represents the xy or equator plane and the associated green vectors are examples of possible measurement axis that can be selected in the sequence depicted in figure 4.1.

photon entangled state can be written as:

$$\rho_{NV,\gamma} = \alpha \left|01\right\rangle \left\langle 01\right| + (1-\alpha) \left|10\right\rangle \left\langle 10\right| + \sqrt{\alpha(1-\alpha)}(\left|01\right\rangle \left\langle 10\right| + \left|10\right\rangle \left\langle 01\right|) \tag{4.1}$$

Then, we simply measure the NV state and ignore the photon state, therefore losing information. In order to simulate what results we expect from this measurement, we need to isolate the NV density matrix, using the partial trace over the photon state, which means that the spin state becomes mixed. More specifically:

$$\begin{aligned} \rho_{NV} &= \left\langle 0_\gamma\right| \rho \left|0_\gamma\right\rangle + \left\langle 1_\gamma\right| \rho \left|1_\gamma\right\rangle \\ &= \begin{pmatrix} \alpha & 0 \\ 0 & 1-\alpha \end{pmatrix} \end{aligned} \tag{4.2}$$

In this case, ρ_{NV} is a diagonal matrix, which means that we lose all coherence in the process and end up with a classical mixture. If we measure the fidelity of the NV's state with respect to the $|0\rangle$ state through the equator plane, we should expect a flat line, as depicted in figure 4.3. However, performing this sequence experimentally, persistently, yielded a consistent oscillation signature that disagreed with this prediction and seemed to indicate that we weren't considering the full picture in our predictions.

4.1 Simulation

We hypothesised that the optical pulse didn't fully saturate the optical transition between the NV's $|0\rangle$ and $|e\rangle$ states. To understand what this means, it is important to clarify that this operation occurs through the same process as the control of the NV when MW pulses are used, i.e., Rabi oscillations. This means

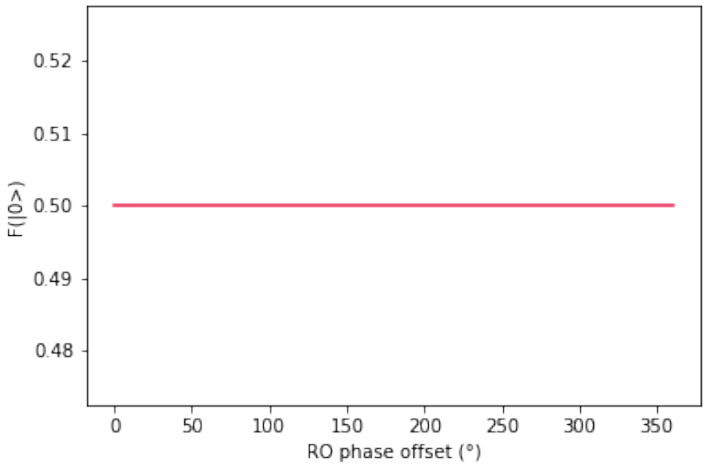

Figure 4.3: Fidelity with respect to the NV's $|0\rangle$ state as a function of the read out (RO) phase in the xy of the Bloch sphere. The 0° phase corresponds to the positive x axis. For the ideal case we loose all coherence, expecting a flat line.

that if we send a pulse resonant with the energy difference associated with the $|0\rangle \leftrightarrow |e\rangle$ transition, the process that follows can be seen as a rotation in the Bloch sphere defined by the two-level system $|0\rangle$, $|e\rangle$, in which the angle of rotation, θ, will depend on the power and length of the pulse.

Ideally, the optical pulse makes a π rotation and excites the entire population from the $|0\rangle$ to the $|e\rangle$ state. However, the hypothesis we want to test is that this angle of rotation is not exactly π, as we aimed for. Instead, we considered the effect of the optical pulse to be described by the following transformations:

$$\begin{aligned} |0\rangle &\rightarrow \cos\frac{\theta}{2}|0\rangle + \sin\frac{\theta}{2}|e\rangle \\ |1\rangle &\rightarrow |1\rangle \end{aligned} . \tag{4.3}$$

Upon resonant excitation, the excited state population will decay back to the lower energy level, after the optical lifetime of 12 ns, emitting a photon. In other words, once applied the optical pulse, the NV emits a photon with probability $p = |\sin\frac{\theta}{2}|^2$. Considering that the NV is prepared in a superposition state with bright state population α, the entangled state between the NV and the photon, after the optical pulse is applied, can be described by equation 4.4

$$|NV\rangle|\gamma\rangle = \sqrt{\alpha}|0\rangle\left(\cos\frac{\theta}{2}|0\rangle + \sin\frac{\theta}{2}|1\rangle\right) + \sqrt{1-\alpha}|1\rangle|0\rangle \tag{4.4}$$

Proceeding again with the partial trace over the photon state (eq. 4.2), we are able to calculate the NV's density matrix. If we then simulate the probability of measuring states in the xy plane of the Bloch sphere, for different values of θ, in an attempt to compare the data with the ideal case represented in figure 4.3, we obtain the plot in figure 4.4.

When no optical pulse is applied, i.e., $\theta = 0$, we see an oscillation with a very large amplitude, since we are essentially measuring the NV in the $|+\rangle$ state (superposition state in which the NV was prepared).

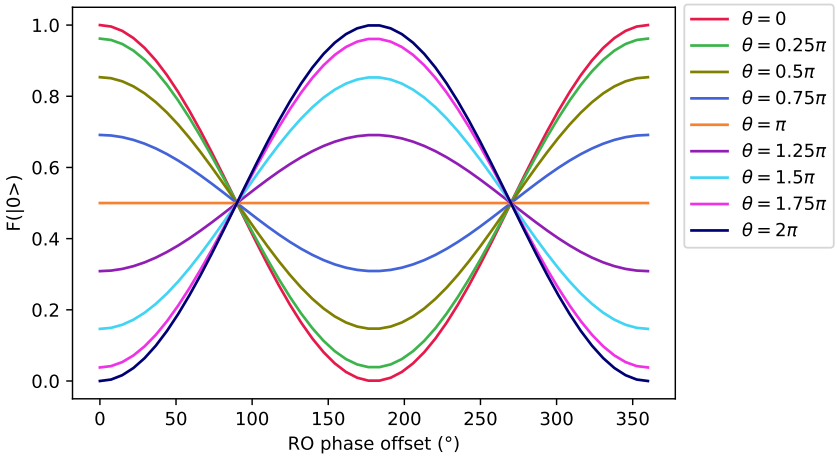

Figure 4.4: Simulation of the fidelity with respect to the NV's $|0\rangle$ state as a function of the RO phase in the xy of the Bloch sphere, for different optical pulse rotation angles, θ (represented in different colors). The 0° RO phase offset corresponds to the positive x axis.

As we increase the angle of rotation, θ, the oscillations tend to vanish, i.e., the amplitude decreases, up to the point that the ideal optical π pulse is reached and the probability of measuring the state with eigenvalue $\lambda = +1$, all over the xy plane is $\frac{1}{2}$ no matter what read out phase is picked. Therefore, for this ideal case, we can say that, once the photon state is "measured" by the environment, the NV is projected to either $|0\rangle$ or $|1\rangle$ and all the coherence disappears.

As we continue to increase θ the oscillations reappear with a phase flip of 180°, which can be explained by an over rotation, i.e., for large pulse powers, we might be driving a the optical transition by $\theta > \pi$, instead of π, as we intended. In a normal situation this rotation would originate a global phase that could be neglected, but since we are now considering a three level system - $|0\rangle$, $|e\rangle$ and $|1\rangle$ - a phase acquired by a 2π rotation between the $|0\rangle$ and $|e\rangle$ states, will turn into a relative phase between the qubit states $|0\rangle$ and $|1\rangle$.

In order to have a clearer and more succinct idea on what is happening to the NV's electron spin state when we change the power of the optical pulse, we resort to the amplitude, A, and phase, ϕ, of the cosine curves simulated in figure 4.4 and calculate the x and y coordinates on the Bloch sphere of the NV's spin state vector, simply using equations 4.5.

$$\begin{cases} x = 2A\cos\phi \\ y = 2A\sin\phi \end{cases} \tag{4.5}$$

In this representation (see figure 4.5), for $\theta = 0$ we should measure the $|+\rangle$ state, i.e., the coordinates of the state vector should be $\{x, y\} = \{1, 0\}$, which corresponds to the superposition state with bright state population $\alpha = 0.5$ that was prepared before the optical pulse. As we increase θ, the Bloch vector length should decrease and the electron spin state coordinates should follow the negative direction of the x axis towards the centre of the equator plane of the Bloch sphere. When $\theta = \pi$ the NV's state should be projected into the z axis of the Bloch sphere that, when observed from the top, should correspond to

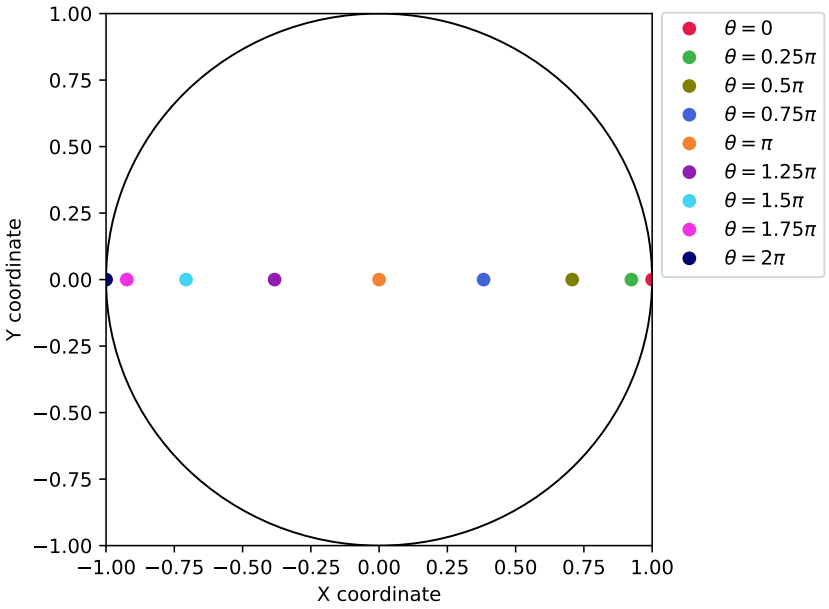

Figure 4.5: Top view Bloch sphere representation of the measured NV's electron spin state vector x and y coordinates after applying the sequence in figure 4.1 with $\alpha = 0.5$.

a point at $\{x, y\} = \{0, 0\}$. As we continue to increase θ, the state vector coordinates should continue to follow the negative direction of the x axis until $\theta = 2\pi$ and we reach $\{x, y\} = \{-1, 0\}$.

In short, the simulations show some residual coherence for imperfect optical pulses, i.e., for angles of rotation $\theta \neq \pi$, which is in agreement with our hypothesis. However, we haven't measured this effect for multiple angles of rotations, θ, and we've never reached the no oscillations point. Therefore, even though it is a plausible explanation for the observed oscillations, it is hard to claim that the proposed hypothesis is confirmed, simply holding this information. Additionally, even if we assume the hypothesis to be true, we are clearly not correctly calibrating the power of the optical pulse, otherwise we wouldn't have observed any oscillations in the first place. Consequently, it is of our best interest to reproduce the simulations with experimental data, not only to determine the validity of our hypothesis but also to find at what power we can produce the optical π pulse and eliminate the oscillations altogether.

4.2 Experimental verification

In an attempt to definitely confirm the hypothesis proposed in the previous section, we experimentally performed the sequence illustrated in figure 4.1 (with $\alpha = 0.5$) for different AOM amplitudes[1] and fitted the results to the function:

$$y(x) = A \cdot \cos(x - \phi) + A_0, \tag{4.6}$$

with $A_0 = 0.5$ fixed.

The quantum network used throughout this project comprises three different nodes and two different

[1] AOM amplitude refers to the amplitude of the signal sent to the RF source that will then output an oscillating electrical signal to the AOM. Therefore, the AOM amplitude is related to the optical excitation pulse power. For the values we use in this section there are two regimes: 1) the power increases with the AOM amplitude; 2) the power is saturated and the increase of the AOM amplitude no longer has an effect on it.

excitation pulses. In order to succeed at three node entanglement experiments, we need to be able to generate high fidelity entanglement between nodes A and B - long distance entanglement (LDE) 1 - and also between nodes B and C - LDE 2. The same optical pulse is used to excite the two nodes that will become entangled. More specifically, when we want entangle nodes A and B, we use optical pulse 1 and when we want to entangle nodes A and C, we use optical pulse 2. This creates a necessity for both pulses to be calibrated in order to perform three-node entanglement. Therefore, if we want to ensure a high fidelity three-node entangled state, both entanglement pairs need to be improved and for that reason, the hypothesis needs to be tested for both entanglement pairs, each pair associated with two nodes and one optical pulse. However, since the same discussion can be applied to both links, both in this chapter and in chapter 5, we will focus on the experimental results associated with link B-C, leaving the identical results regarding the other link, A-B, to be depicted in appendix C, to avoid redundancy.

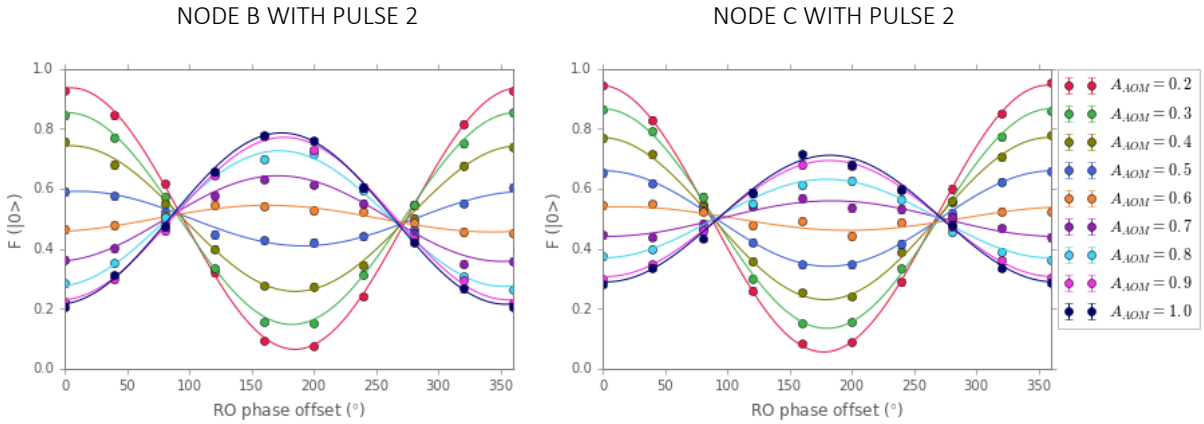

Figure 4.6: Fit of the function 4.6 to the experimental points after applying the sequence in figure 4.1 with $\alpha = 0.5$. The y axis of the plot corresponds to the fidelity of the NV's electron spin state with the $|0\rangle$ state, after a rotation to the right read out basis, while the x axis corresponds to the read out phase in the xy of the Bloch sphere. The $0°$ RO phase corresponds to the positive x axis. The different colors correspond to different AOM amplitudes that are related to power of the optical pulse.

As we can see in figure 4.6, the experimental results resemble the simulation's, given that a clear sinusoidal behavior and a 180° phase flip are observed for both entanglement pairs. However, we never see the flat line that is expected in the ideal case, suggesting that the optical pulses that drive the $|0\rangle \rightarrow |e\rangle$ transition, are never equivalent to perfect π rotations for any of the measured points.

Once again, displaying the evolution of the NV's electron spin state as a function of the power of the optical pulse, in a more intuitive representation, we resort to the amplitude, A, and phase, ϕ, parameters obtained from the fit of the function 4.6 to the experimental points displayed on figure 4.6 and calculate the x and y components of the NV's spin state vector, simply using equations 4.5.

The behaviour simulated in figure 4.5 is indeed what we observe when analysing the data points for both entanglement pairs, in figure 4.7. The NV's state vector coordinate starts at some point with positive x coordinate and $y \approx 0$ and, as we increase the delivered power (governed by an increase of the AOM amplitude), it follows the negative direction of the x axis, passing through the center of the xy plane of the Bloch sphere. Although we don't measure the exact point corresponding to $\theta = \pi$, we see that it is merely a problem of the selected power sweep points, i.e., the perfect π pulse is somewhere in

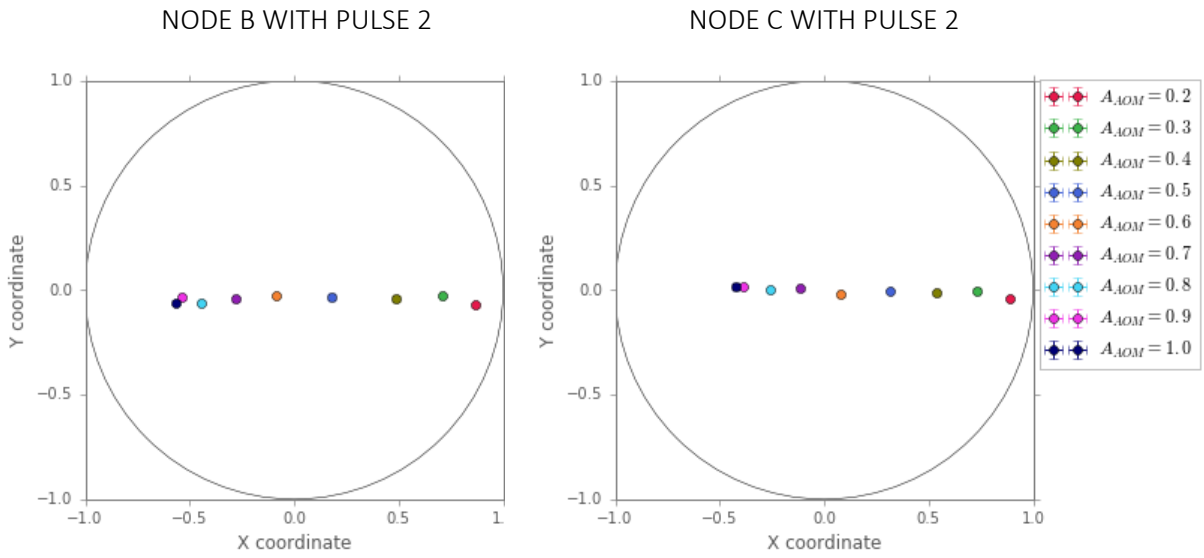

Figure 4.7: Top view Bloch sphere representation of the measured NV's electron spin state vector x and y coordinates after applying the sequence in figure 4.1 with $\alpha = 0.5$.

between the $A_{AOM} = 0.5$ and $A_{AOM} = 0.7$ and we should be able to reach it within uncertainty.

In conclusion, the experimental data validates the hypothesis that the oscillations observed when measuring the NV's electron spin state, after being entangled with a photon state, were caused by a non perfect excitation pulse that can be easily improved with an accurate calibration. Nonetheless, an error in the excitation pulse means that from the absence of a photon we can no longer infer that the NV is in the $|1\rangle$ state and thus, the spin-photon entangled state, on which the two-node entanglement relies on, is not what we initially assumed. Consequently, it is important to study the effect of a non perfect excitation pulse on the fidelity of the final spin-spin entangled state, such that we can comprehend how accurate this extra calibration step need to be.

Chapter 5

Study of the spin-spin entanglement fidelity and generation rate

We are now able to identify the source of the oscillations and claim that the calibration of the optical pulse (see section 4.2) is slightly inaccurate for the simple reason that it led to a misidentification of the power at which a perfect excitation occurs. In other words, it didn't allow us to find the power of the optical pulse, that used in the sequence illustrated in figure 4.1, would have projected the NV's state vector somewhere (depending on α) along the z axis and, consequently, when observed from the top of the Bloch sphere (see figure 4.5) seen as a point exactly at the middle of the xy plane. Consequently, the following step is to determine to what degree this imperfection affects the final spin-spin entangled state, so we know how accurately we need to set the excitation pulse power in order to guarantee the fidelity is not affected.

5.1 System's characterization

In this section, we present the complete derivation of the fidelity and rate expressions and study their dependence on the rotation angle of the optical pulse, θ. Other sources of infidelity have been studied and considered in previous works [31], when simulating the fidelity of the final spin-spin entangled state. Nonetheless, in this section, we will simply focus on the imperfections of the optical pulse, while also taking losses and non-number resolution detectors into account, leaving the remaining details for later.

5.1.1 Derivation of the fidelity and rate

To make this derivation as general as possible within the purpose of this section, we consider the two nodes to be imbalanced, i.e., for each free parameter associated with node A, there is an analogous free parameter associated with node B. This is important because it allows a more rigorous simulation of the experiment, since the three nodes we have at our disposal are not exactly the same. All three set ups will naturally differ in certain aspects, making it unfair to restrict this investigation to the unrealistic

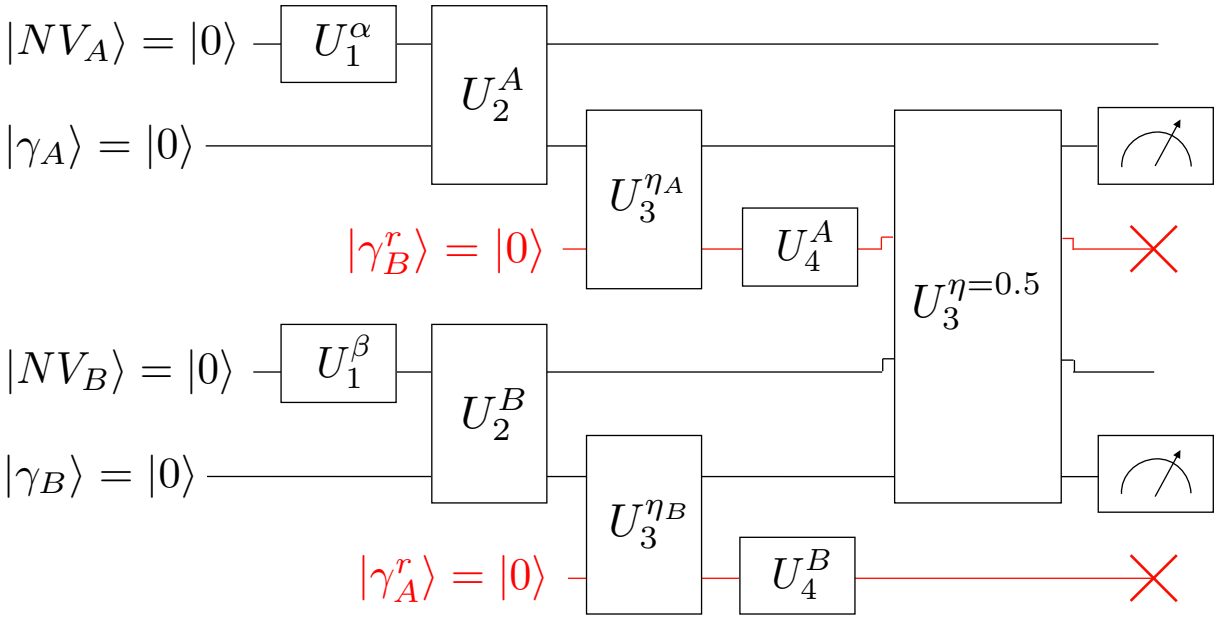

Figure 5.1: Characterization of our system's time evolution when two-node entanglement is attempted, in the form of a quantum circuit. Each box corresponds to a unitary transformation that is properly characterized throughout this section, with the exception of the last two boxes that represent a measurement. The circuit is to be read from left to right. Six different quantum states are represented - $|NV_A\rangle$ and $|NV_B\rangle$ that correspond to the electron spin state of nodes A and B, respectively; $|\gamma_A\rangle$ and $|\gamma_B\rangle$ that correspond to the number of photons in channels γ_A and γ_B that lead to the single photon detectors 1 and 2 (see figure 5.2), respectively; $|\gamma_A^r\rangle$ and $|\gamma_B^r\rangle$ that correspond to the presence/absence of a photon in the loss channels γ_A^r and γ_B^r. The circuit starts with all six states initialized in $|0\rangle$. Then, U_1^j, describing the spin evolution resulting from a MW pulse, brings the NV's to a superposition state. It follows U_2^j that characterizes the effect of the optical pulse and entangles each NV_j with a photon state $|\gamma_j\rangle$. Later, $U_3^{\eta_j}$ expresses the losses associated with node j and $U_3^{\eta=0.5}$ portrays the photon interference between channels γ_A and γ_B at the central 50:50 beam splitter. Finally, the photons in these two channels will be measured and a spin-spin entangled state is heralded once one of the detectors records an event. The red crosses represent a partial trace over those specific quantum states, given that we have no way of determining them.

case of perfectly identical setups. Accordingly, we can start the derivation by considering two nodes, A and B, to be both initialized in the $|0\rangle$ state and proceed to the characterization of the MW pulse, as the subsequent step in the sequence of figure 4.1. For that, we rely on the unitary transformation U_1^j, such that each NV electron spin state is transformed as

$$U_1^j : |0\rangle_{NV} \rightarrow \sqrt{j}\,|0\rangle_{NV} + \sqrt{1-j}\,|1\rangle_{NV}\,, \tag{5.1}$$

ending up in a superposition state with bright state populations α and β in the case of node A and B, respectively. The corresponding joint state can be described by equation 5.2.

$$\begin{aligned} |\Psi_1\rangle_{NV_A,NV_B} &= \underbrace{(U_1^\alpha\,|0\rangle_{NV_A})}_{|\Psi_1\rangle_{NV_A}} \otimes \underbrace{(U_1^\beta\,|0\rangle_{NV_B})}_{|\Psi_1\rangle_{NV_B}} \\ &= \left(\sqrt{\alpha}\,|0\rangle_{NV_A} + \sqrt{(1-\alpha)}\,|1\rangle_{NV_A}\right) \otimes \left(\sqrt{\beta}\,|0\rangle_{NV_B} + \sqrt{(1-\beta)}\,|1\rangle_{NV_B}\right) \end{aligned} \tag{5.2}$$

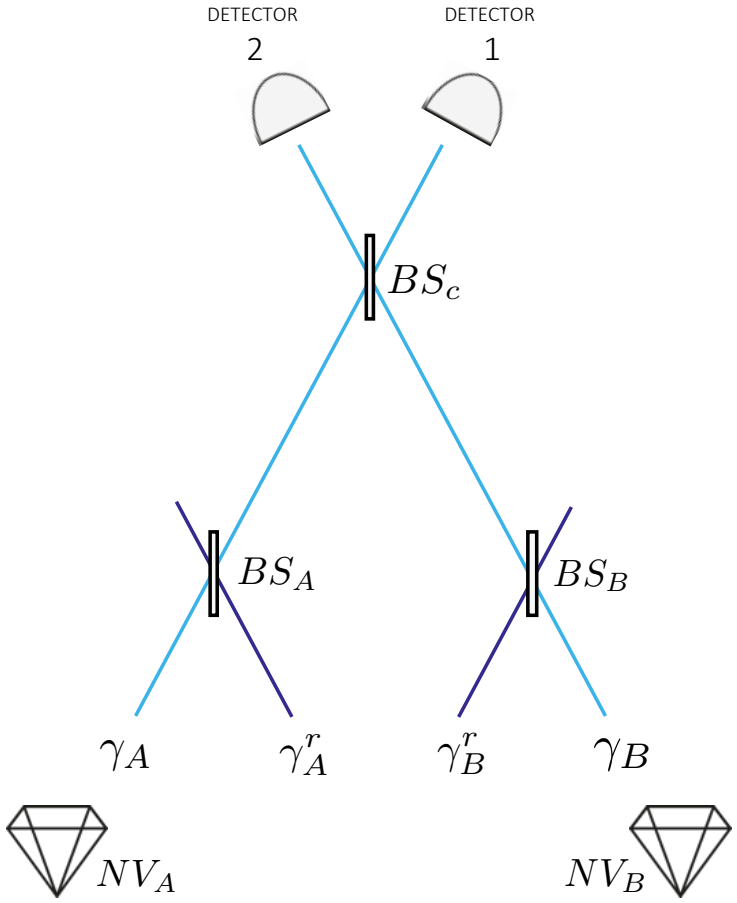

Figure 5.2: Schematic overview of the single click entanglement modelling. Channels γ_A and γ_B are physical channels that connect NV_A and NV_B to detectors 1 and 2, respectively. Channels γ_A^r and γ_B^r correspond to the loss channels that, along with beam splitters BS_A and BS_B, model the photon losses that naturally occur in experiments. BS_c corresponds to the central beam splitter in which the photons in channels γ_A and γ_B interfere.

Then, as the optical pulse is applied to each node, a fraction of the population in the $|0\rangle_{NV_j}$ state is transferred to the $|e\rangle_{NV_j}$ state, leaving the $|1\rangle_{NV_j}$ state intact. Such an excitation process can be pictured as a rotation of an angle θ_j in the Bloch sphere, defined by the $\{|0\rangle_{NV_j}, |e\rangle_{NV_j}\}$ basis. Accordingly, the fraction of the population that gets excited is equal to $\left|\sin\frac{\theta_j}{2}\right|^2$, where θ_j is experimentally determined by the pulse's power and length. Upon the decay of the $|e\rangle_{NV_j}$ state population back to the ground state, $|0\rangle_{NV_j}$, a subsequent photon is emitted into channel γ_j (see figure 5.2). In other words, the expanded system, $|\Psi_2\rangle = |\Psi_1\rangle\,|\gamma_A\rangle\,|\gamma_B\rangle$, we are now describing, which assembles not only both NV's electron spin states but also the presence/absence of photons in channels γ_A and γ_B, is mathematically transformed by the optical pulse according to the unitary transformation, U_2^j, that can be written as:

$$U_2^j : \begin{cases} |0\rangle_{NV_j}\,|0\rangle_{\gamma_j} \rightarrow \cos\frac{\theta_i}{2}\,|0\rangle_{NV_j}\,|0\rangle_{\gamma_j} + \sin\frac{\theta_j}{2}\,|0\rangle_{NV_j}\,|1\rangle_{\gamma_j} \\ |1\rangle_{NV_j}\,|0\rangle_{\gamma_j} \rightarrow |1\rangle_{NV_j}\,|0\rangle_{\gamma_j} \end{cases} . \tag{5.3}$$

We can proceed to write the joint state of the transformed system:

$$
\begin{aligned}
|\Psi_3\rangle &= \underbrace{\left[U_2^A\left(|\Psi_1\rangle_{NV_A}|0\rangle_{\gamma_A}\right)\right]}_{|\Psi_3\rangle_A} \otimes \underbrace{\left[U_2^B\left(|\Psi_1\rangle_{NV_B}|0\rangle_{\gamma_B}\right)\right]}_{|\Psi_3\rangle_B} \\
&= \left[\left(\sqrt{\alpha}\cos\frac{\theta_A}{2}|0\rangle_{NV_A} + \sqrt{1-\alpha}|1\rangle_{NV_A}\right)|0\rangle_{\gamma_A} + \sqrt{\alpha}\sin\frac{\theta_A}{2}|0\rangle_{NV_A}|1\rangle_{\gamma_A}\right] \\
&\otimes \left[\left(\sqrt{\beta}\cos\frac{\theta_B}{2}|0\rangle_{NV_B} + \sqrt{1-\beta}|1\rangle_{NV_B}\right)|0\rangle_{\gamma_B} + \sqrt{\beta}\sin\frac{\theta_B}{2}|0\rangle_{NV_B}|1\rangle_{\gamma_B}\right].
\end{aligned}
\tag{5.4}
$$

Equation 5.4 highlights that, in this derivation, the spin-photon entangled state is no longer characterized by equation 2.6, as initially suggested in section 2.3.1, but instead, it is generalized to equation 4.4, that nicely agrees with the experimental data analysed in section 4.2.

Furthermore, since the setups are subject to significant losses (photons that are emitted but not detected), it is important to understand how we can mathematically describe them. First, it is important to note that we treat these losses as if they all occurred before the central beam splitter and describe them using η, defined as the fraction of emitted photons that are detected. To support this assumption, we identify where the losses take place. Some of them result from photon emission in the phonon side band, i.e., the emitted photons' frequency doesn't correspond to the frequency associated with the $|0\rangle \leftrightarrow |e\rangle$ optical transition. Given that a requirement for the single click entanglement scheme is the indistinguishably of the photons, we can only use, for entanglement purposes, the photons emitted in the zero-phonon sideband, with a very well defined frequency, corresponding only to 3% of the emissions. Therefore, this effect alone, leads to a 97% loss. Additionally, as described in section 3.1, even with the solid immersion lens (SIL) fabricated around the NV to maximize the photon collection, the fraction of photons that end up being collected is limited by the numerical aperture of the microscope objective (also responsible for the focusing of the laser light onto the NV, as mentioned in section 3.2), therefore decreasing even more the photon detection probability. Finally, the coupling of the emitted light into the single mode fibers that guide the photons to the central beam splitter is not perfect. All these losses occur before the central beam splitter. After this component, the only significant loss is due to the non-perfect efficiency of the detectors, which is around 95$\%$ - a negligible value to what the previous causes account for. Consequently, we can proceed to model the losses as two extra beam splitters, BS_A and BS_B, placed before the central beamsplitter, BS_c, that can either reflect (loss term) or transmit the input photons, as illustrated in figure 5.2. More specifically, we consider single dielectric layer $\eta_j : (1-\eta_j)$ beam splitters that transform any two interfering channels γ_1 and γ_2 through the unitary $U_3^{\eta_j}$ (equation 5.5), where η_j corresponds to the fraction of input photons that are transmitted through BS_j. To treat it quantum mechanically, we may consider a system, $|\Psi_4\rangle = |\Psi_2\rangle|\gamma_A^r\rangle|\gamma_B^r\rangle$, that includes both NV's electron spin states and the presence/absence of photons in channels γ_A and γ_B - transmitted photons - and channels γ_A^r and γ_B^r - reflected photons - and use the unitary transformation $U_3^{\eta_j}$ to relate the input and output modes of the considered channels as [32]:

$$U_3^{\eta_j}:\begin{cases}|0\rangle_{\gamma_1^{in}}|0\rangle_{\gamma_2^{in}}\rightarrow|0\rangle_{\gamma_1^{out}}|0\rangle_{\gamma_2^{out}}\\ |0\rangle_{\gamma_1^{in}}|1\rangle_{\gamma_2^{in}}\rightarrow\sqrt{\eta_j}\,|0\rangle_{\gamma_1^{out}}|1\rangle_{\gamma_2^{out}}+i\sqrt{1-\eta_j}\,|1\rangle_{\gamma_1^{out}}|0\rangle_{\gamma_2^{out}}\\ |1\rangle_{\gamma_1^{in}}|0\rangle_{\gamma_2^{in}}\rightarrow i\sqrt{1-\eta_j}\,|0\rangle_{\gamma_1^{out}}|1\rangle_{\gamma_2^{out}}+\sqrt{\eta_j}\,|1\rangle_{\gamma_1^{out}}|0\rangle_{\gamma_2^{out}}\\ |1\rangle_{\gamma_1^{in}}|1\rangle_{\gamma_2^{in}}\rightarrow(2\eta_j-1)\,|1\rangle_{\gamma_1}|1\rangle_{\gamma_2}+i\sqrt{\eta_j(1-\eta_j)}(|0\rangle_{\gamma_1}|2\rangle_{\gamma_2}+|2\rangle_{\gamma_1}|0\rangle_{\gamma_2})\end{cases}. \tag{5.5}$$

Additionally, knowing the photons in channels γ_A and γ_B will later interfere at the central beam splitter, it is necessary to consider the different optical phases, ϕ_A and ϕ_B, respectively, associated with each path-length, acquired by an electromagnetic wave travelling through each channel. This particular evolution of the system can be characterized by the unitary transformation

$$U_4^j:\begin{cases}|0\rangle_{\gamma_j}\rightarrow|0\rangle_{\gamma_j}\\ |1\rangle_{\gamma_j}\rightarrow e^{i\phi_j}|1\rangle_{\gamma_j}\end{cases}, \tag{5.6}$$

which can be further used to describe the system's state right before the photons arrive at the central beam splitter, BS_c, as

$$\begin{aligned}|\Psi_5\rangle&=\left[U_4^A\left(U_3^{\eta_A}|\Psi_3\rangle_A|0\rangle_{\gamma_A^r}\right)\right]\otimes\left[U_4^B\left(U_3^{\eta_B}|\Psi_3\rangle_B|0\rangle_{\gamma_B^r}\right)\right]\\ &=\left[\left(\sqrt{\alpha}\cos\frac{\theta_A}{2}|0\rangle_{NV_A}+\sqrt{1-\alpha}\,|1\rangle_{NV_A}\right)|0\rangle_{\gamma_A}|0\rangle_{\gamma_A^r}\right.\\ &\quad\left.+\sqrt{\alpha}\sin\frac{\theta_A}{2}|0\rangle_{NV_A}\left(e^{i\phi_A}\sqrt{\eta_A}\,|1\rangle_{\gamma_A}|0\rangle_{\gamma_A^r}+i\sqrt{1-\eta_A}\,|0\rangle_{\gamma_A}|1\rangle_{\gamma_A^r}\right)\right]\otimes\\ &\quad\left[\left(\sqrt{\beta}\cos\frac{\theta_B}{2}|0\rangle_{NV_B}+\sqrt{1-\beta}\,|1\rangle_{NV_B}\right)|0\rangle_{\gamma_B}|0\rangle_{\gamma_B^r}\right.\\ &\quad\left.+\sqrt{\beta}\sin\frac{\theta_B}{2}|0\rangle_{NV_B}\left(e^{i\phi_B}\sqrt{\eta_B}\,|1\rangle_{\gamma_B}|0\rangle_{\gamma_B^r}+i\sqrt{1-\eta_B}\,|0\rangle_{\gamma_B}|1\rangle_{\gamma_B^r}\right)\right],\end{aligned} \tag{5.7}$$

considering the channel correspondence $|\gamma_1\rangle|\gamma_2\rangle=|\gamma_j\rangle|\gamma_j^r\rangle$, with $j=\{A,B\}$, when using unitary $U_3^{\eta_j}$.

Moreover, the photons transmitted through BS_A and BS_B will interfere at the central 50:50 beam splitter, which means we can rely once again on transformation $U_3^{\eta_i}$, but this time considering $\eta_i=\frac{1}{2}$ and the interfering channels to be $|\gamma_1\rangle|\gamma_2\rangle=|\gamma_A\rangle|\gamma_B\rangle$. The final state of the entire system before the

excitation photons reach the detectors can be written as

$$
\begin{aligned}
|\Psi_6\rangle = &\left[\left(\sqrt{\alpha}\cos\frac{\theta_A}{2}|0\rangle_{NV_A} + \sqrt{1-\alpha}\,|1\rangle_{NV_A}\right)|0\rangle_{\gamma_A^r} + i\sqrt{\alpha(1-\alpha)}\sin\frac{\theta_A}{2}e^{i\phi_A}|0\rangle|1\rangle_{\gamma_A^r}\right]\otimes \\
&\left[\left(\sqrt{\beta}\cos\frac{\theta_B}{2}|0\rangle_{NV_B} + \sqrt{1-\beta}\,|1\rangle_{NV_B}\right)|0\rangle_{\gamma_B^r} + i\sqrt{\beta(1-\beta)}\sin\frac{\theta_B}{2}e^{i\phi_B}|0\rangle|1\rangle_{\gamma_B^r}\right]|0\rangle_{\gamma_A}|0\rangle_{\gamma_B} \\
+ &\frac{e^{i\phi_B}}{\sqrt{2}}\left[\left(\sqrt{\alpha}\cos\frac{\theta_A}{2}|0\rangle_{NV_A} + \sqrt{1-\alpha}\,|1\rangle_{NV_A}\right)\otimes\left(\sqrt{\beta\eta_B}\sin\frac{\theta_B}{2}|0\rangle_{NV_B}\right)|0\rangle_{\gamma_A^r}|0\rangle_{\gamma_B^r} + \right. \\
&\left.\left(\sqrt{\alpha(1-\eta_A)}\sin\frac{\theta_A}{2}|0\rangle_{NV_A}\right)\otimes\left(\sqrt{\beta\eta_B}\sin\frac{\theta_B}{2}|0\rangle_{NV_B}\right)|1\rangle_{\gamma_A^r}|0\rangle_{\gamma_B^r}\right]\left(|0\rangle_{\gamma_A}|1\rangle_{\gamma_B} + i\,|1\rangle_{\gamma_A}|0\rangle_{\gamma_B}\right) \\
+ &\frac{e^{i\phi_A}}{\sqrt{2}}\left[\left(\sqrt{\alpha\eta_A}\sin\frac{\theta_A}{2}|0\rangle_{NV_A}\right)\otimes\left(\sqrt{\beta}\cos\frac{\theta_B}{2}|0\rangle_{NV_B} + \sqrt{1-\beta}\,|1\rangle_{NV_B}\right)|0\rangle_{\gamma_A^r}|0\rangle_{\gamma_B^r} + \right. \\
&\left.\left(\sqrt{\alpha\eta_A}\sin\frac{\theta_A}{2}|0\rangle_{NV_A}\right)\otimes\left(\sqrt{\beta(1-\eta_B)}\sin\frac{\theta_B}{2}|0\rangle_{NV_B}\right)|0\rangle_{\gamma_A^r}|1\rangle_{\gamma_B^r}\right]\left(i\,|0\rangle_{\gamma_A}|1\rangle_{\gamma_B} + |1\rangle_{\gamma_A}|0\rangle_{\gamma_B}\right) \\
+ &\left[\frac{i}{\sqrt{2}}e^{i(\phi_A+\phi_B)}\left(\sqrt{\alpha}\sin\frac{\theta_A}{2}\sqrt{\eta_A}|0\rangle_{NV_A}\right)\otimes\left(\sqrt{\beta}\sin\frac{\theta_B}{2}\sqrt{\eta_B}|0\rangle_{NV_B}\right)\right]|0\rangle_{\gamma_A^r}|0\rangle_{\gamma_B^r}\left(|0\rangle_{\gamma_A}|2\rangle_{\gamma_B} + |2\rangle_{\gamma_A}|0\rangle_{\gamma_B}\right)
\end{aligned}
\tag{5.8}
$$

Finally, one of the detectors records an event and we can identify two different situations that can lead to this event:

- Only one photon arrived at the detector. In this case the detected modes are projected onto $|1\rangle_{\gamma_A}|0\rangle_{\gamma_B}$ ($|0\rangle_{\gamma_A}|1\rangle_{\gamma_B}$) if detector 1 (2) clicks. This situation can happen either because only one of the NV's was excited and emitted a photon that ended up being detected or because both NV's were excited and emitted a photon each, but only one photon arrived at the detector, since the other one was lost. The un-normalized system will then be described as[1]

$$
\begin{aligned}
|\Psi_7\rangle &= \begin{cases}\left(\langle 1|_{\gamma_A}\langle 0|_{\gamma_B}\right)|\Psi_6\rangle\text{, if } detector = 1\\ \left(\langle 0|_{\gamma_A}\langle 1|_{\gamma_B}\right)|\Psi_6\rangle\text{, if } detector = 2\end{cases} \\
&= \left[\left(\sqrt{\alpha}\cos\frac{\theta_A}{2}|0\rangle_{NV_A} + \sqrt{1-\alpha}\,|1\rangle_{NV_A}\right)|0\rangle_{\gamma_A^r} + \sqrt{\alpha(1-\eta_A)}\sin\frac{\theta_A}{2}|0\rangle_{NV_A}|1\rangle_{\gamma_A^r}\right]\otimes \\
&\left(e^{i\phi_B}\sqrt{\beta\eta_B}\sin\frac{\theta_B}{2}|0\rangle_{NV_B}|0\rangle_{\gamma_B^r}\right) + i(-1)^{detector}\left(e^{i\phi_A}\sqrt{\alpha\eta_A}\sin\frac{\theta_A}{2}|0\rangle_{NV_A}|0\rangle_{\gamma_A^r}\right)\otimes \\
&\left[\left(\sqrt{\beta}\cos\frac{\theta_B}{2}|0\rangle_{NV_B} + \sqrt{1-\beta}\,|1\rangle_{NV_B}\right)|0\rangle_{\gamma_B^r} + \sqrt{\beta(1-\eta_B)}\sin\frac{\theta_B}{2}|0\rangle_{NV_B}|1\rangle_{\gamma_B^r}\right]
\end{aligned}
\tag{5.9}
$$

- Two photons arrived at the detector because both NV's were excited and no loss occurred. In this case, the detected modes are projected onto $|2\rangle_{\gamma_A}|0\rangle_{\gamma_B}$ ($|0\rangle_{\gamma_A}|2\rangle_{\gamma_B}$) if detector 1 (2) clicks. The un-normalized system will then be described as[1]

[1] Generally, the collapse of a wave function $|\Psi\rangle$ is represented as $P|\Psi\rangle$, where P is a matrix form projector, i.e., $P = |b\rangle\langle b|$ where $|b\rangle$ is the basis we want our system to be projected onto. For the sake of simplicity, we project our system in a way that its dimension is reduced from six to four sub-systems. Given that, in the end, we are only interested in the NV's states, this way we avoid having to redundantly specify the $|\gamma_A\rangle|\gamma_B\rangle$ states that were previously projected.

$$
\begin{aligned}
|\Psi_8\rangle &= \begin{cases} \left(\langle 2|_{\gamma_A} \langle 0|_{\gamma_B}\right) |\Psi_6\rangle \text{ , if } detector = 1 \\ \left(\langle 0|_{\gamma_A} \langle 2|_{\gamma_B}\right) |\Psi_6\rangle \text{ , if } detector = 2 \end{cases} \\
&= \left(e^{i\phi_A}\sqrt{\alpha\eta_A}\sin\frac{\theta_A}{2}|0\rangle_{NV_A}|0\rangle_{\gamma_A^r}\right) \otimes \left(e^{i\phi_B}\sqrt{\beta\eta_B}\sin\frac{\theta_B}{2}|0\rangle_{NV_B}|0\rangle_{\gamma_B^r}\right)
\end{aligned} \tag{5.10}
$$

Since the single photon detectors cannot distinguish between one or more photons arriving at the same time, we cannot distinguish between these two situations. Additionally, given the lost photons end up never being measured, we can trace over the undetected modes, ending up with a density matrix, ρ_1 or ρ_2, that describes the joint state of the NV's, in case one or two photons arrived at the detector, respectively.

$$
\rho_{7,8} = \sum_{i,j=0}^{1} {}_{\gamma_A^r}\,{}_{\gamma_B^r}\langle i\ j|\left(|\Psi_{7,8}\rangle\langle\Psi_{7,8}|\right)|i\ j\rangle_{\gamma_A^r\ \gamma_B^r} \tag{5.11}
$$

Finally, we can write the density matrix of the final two-node entangled state as

$$
\rho = \frac{\rho_7 + \rho_8}{p_{click}} \tag{5.12}
$$

where p_{click} corresponds to the probability of succeeding at preparing an entangled state defined as $p_{click} = Tr(\rho_7 + \rho_8)$.

After all these calculations and associated assumptions we can finally explicitly write the two final quantities we are interested in - the fidelity, defined as

$$
\begin{aligned}
\mathcal{F} &= \left\langle \Psi^{target}\right| \rho \left|\Psi^{target}\right\rangle \\
&= \frac{1}{2p_{click}}\left(\alpha(1-\beta)\eta_A\sin^2\frac{\theta_A}{2} + \beta(1-\alpha)\eta_B\sin^2\frac{\theta_B}{2} + 2\sqrt{\alpha(1-\alpha)\eta_A}\sqrt{\beta(1-\beta)\eta_B}\sin\frac{\theta_A}{2}\sin\frac{\theta_B}{2}\right)
\end{aligned} \tag{5.13}
$$

where $|\Psi^{target}\rangle = |01\rangle + e^{i\phi_{target}}|10\rangle$ is the maximally entangled state and the probability of click:

$$
\begin{aligned}
p_{click} = {} & \beta\eta_B\sin^2\frac{\theta_B}{2} + \alpha\eta_A\sin^2\frac{\theta_A}{2} - \alpha\beta\eta_A\eta_B\sin^2\frac{\theta_A}{2}\sin^2\frac{\theta_B}{2} \\
& + 2(-1)^{detector}\alpha\beta\sqrt{\eta_A\eta_B}\cos\Delta\phi\sin\frac{\theta_A}{2}\sin\frac{\theta_B}{2}\cos\frac{\theta_A}{2}\cos\frac{\theta_B}{2}
\end{aligned} \tag{5.14}
$$

with $\Delta\phi = \phi_A - \phi_B - \frac{\pi}{2}$. Although all the eight parameters that define both these quantities have had been mentioned before, the following list shortly clarifies what they all stand for:

- α (β) - bright state population of setup A (B)
- θ_A (θ_B) - angle of rotation of the optical pulse on setup A (B)
- η_A (η_B) - number of photons emitted by setups A (B) that end up being detected

- $\Delta\phi$ - optical phase difference between the optical paths of the two used setups
- $detector$ - (as it self-explains) detector that measures the photon; it can be either equal to 1 or 2

5.1.2 Entanglement fidelity simulation

Going back to the main goal of studying the effect of a faulty optical pulse on the fidelity of the prepared spin-spin entangled state, with regards to the maximally entangled Bell state $|\psi^{target}\rangle$, we can now use equation 5.13 to plot the fidelity as a function of θ_A and/or θ_B , while fixing all the other parameters. To start, let's take the simple case and consider the setups to be balanced, i.e., $\theta_A = \theta_B = \theta$, $\alpha = \beta$, and $\eta_A = \eta_B$. In principle, this is the case we are aiming for because if both setups are exactly the same (even though it's not realistic as mentioned before), then, after a photon passed through the central beam splitter, it is not possible to determine from which setup it was emitted, therefore maximizing the fidelity. Additionally, since there is no special reason to favor any set of parameters, figure 5.3 depicts several plots of the fidelity in different regimes (different α, $\Delta\phi$ and detector values). We also consider $\eta_A = \eta_B = 10^{-4}$, which resembles the experimental conditions.

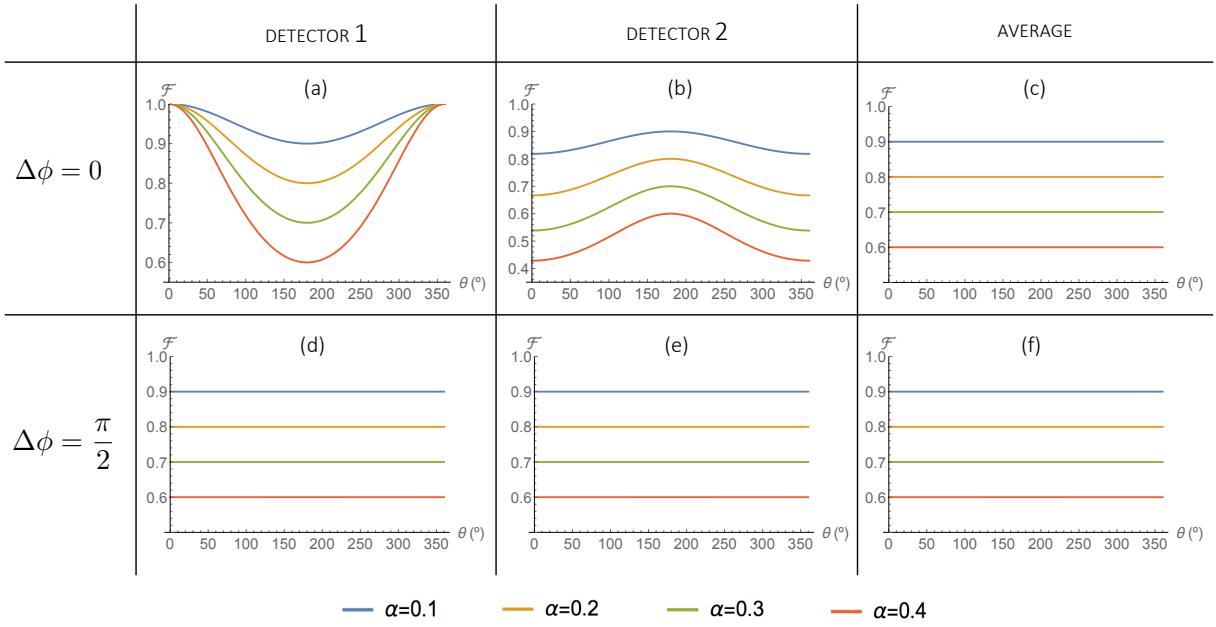

Figure 5.3: Plots of the simulated two-node entangled state fidelity - defined by equation 5.13 in the first two column plots where we consider the case of the heralding photon hitting detector 1 or 2, separately; and defined by equation 5.15 in the last column plots where we take the entire system (both detectors) into account and calculate the weighted average of the first two columns - as a function of the optical pulse rotation angle, $\theta = \theta_A = \theta_B$, in different optical phase difference, $\Delta\phi$, and bright state population, $\alpha = \beta$, regimes. We also considered $\eta_A = \eta_B = 10^{-4}$, similarly to experiments.

Starting by analysing the simulations for $\Delta\phi = \frac{\pi}{2}$, it is clear that the fidelity varies with θ in different ways depending on which detector measured the photon. More specifically, on the contrary to what is observed in figure 5.3(b), in which the maximum fidelity is at $\theta = \pi$, in figure 5.3(a) we are able to reach an increasingly higher fidelity the further away we step from the ideal optical π pulse, the only single difference between these two figures being which detector measured the heralding photon, or in other words, which path the photon followed after the central beam splitter. This observation sparked a certain

curiosity because, in principle, one would expect the fidelity to be either maximum for an ideal π pulse or not depend on θ at all, deserving special analysis further on. Moreover, if we analyse the $\Delta\phi = \frac{\pi}{2}$ plots, the dependence of the fidelity on θ, vanishes, regardless of what detector measured the photon.

When we examine the entire setup and account for all photons that are detected (either by detector 1 our 2) we can calculate the average fidelity as

$$\mathcal{F}_{average} = \mathcal{F}_1 p_{click_1} + \mathcal{F}_2 p_{click_2}, \tag{5.15}$$

$\mathcal{F}_i$ and p_{click_i} being associated with detector i. Although, in case it's beneficial, we can filter out the states heralded by either one of the detectors, the average fidelity is the parameter we usually rely on to validate the experiment, since it takes into account the entire setup, instead of disregarding part of the heralding clicks. In figures 5.3(c) and 5.3(f) the average fidelity, $\mathcal{F}_{average}$, is plotted once again as a function of the angle of rotation of the optical pulse, θ. For both optical phase differences $\Delta\phi = \frac{\pi}{2}$ and $\Delta\phi = 0$, the average fidelity is independent of θ. In other words and answering the question in section 4.2, regarding how accurately the optical pulse needs to be calibrated if high fidelity entangled states are our only concern, in the specific conditions considered in these plots - balanced setups in a high loss regime - it is not important whether the the optical pulse can perfectly excite the NV's $|0\rangle$ state or not.

5.2 Experimental verification

After the development of every model, it is valuable to take experimental data in order to confirm its validity. That is the purpose of this section. In the previous section, the entanglement fidelity and probability of click equations were derived, leading to some theoretical prediction that culminate in figure 5.3. The following step is to verify those same predictions, i.e., we are interested in reproducing what was simulated in figure 5.3 both for $\Delta\phi = 0°$ and $\Delta\phi = 90°$. All the measurements in this section were performed using nodes B and C.

5.2.1 Calibration

The final three quantities we are interested in measuring are the fidelity, $\mathcal{F}$, the probability of preparing an entangled state P_{click} and the rotation of the optical pule, θ. Logically, there is no detector capable of directly measuring these parameters. Therefore, we use the setup at our disposal to calibrate some of them.Then we prepare the same state over and over again such that it can be measured in different basis. After applying the sequence in figure 4.1 to both NV's and measuring a heralding photon, their electron spin states are measured in the xx, yy and zz basis. The results of these measurements allow us to calculate the quantum correlator for each basis, given by:

$$Correlation = \frac{N_{00} - N_{01} - N_{10} + N_{11}}{N_{total}}. \tag{5.16}$$

Then, we are able to calculate the final fidelity as [2]

$$\mathcal{F} = \frac{1 + |<ZZ>| + |<XX>| + |<YY>|}{4} \tag{5.17}$$

In order to find θ, we use the optical pulse saturation calibration (see section A.1.14) that relates the AOM amplitude to the number of detected PSB photons. Afterwards we consider that the number of counts is proportional to the population that was excited to the $|e\rangle$ state, $p_{|e\rangle}$, and normalize, assuming the maximum data point to correspond to the point where the entire population was excited, i.e., $p_{|e\rangle} = 1$. Finally we consider that θ relates to the population in the excited state as

$$p_{|e\rangle} = \sin^2 \frac{\theta}{2} \tag{5.18}$$

and plot the AOM amplitude as a function of θ and fit the data to a polynomial function

$$\theta(A_{AOM}) = a_1 A_{AOM} + a_3 A_{AOM}^3 + a_5 A_{AOM}^5, \tag{5.19}$$

such that we can continuously relate these two quantities.

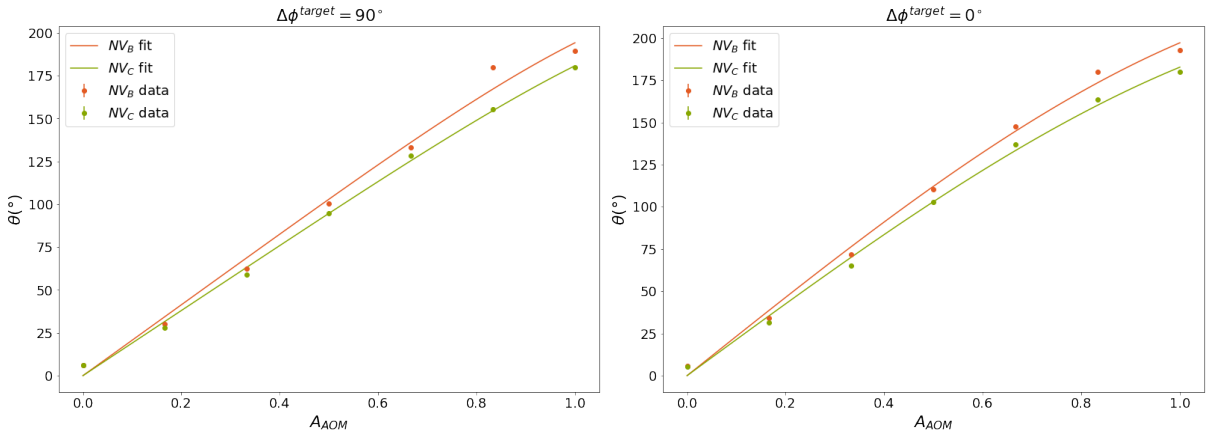

Figure 5.4: Fit of equation 5.19 to the experimental calibration points of θ as a function of the A_{aom}.

Node	$\Delta\phi^{target}$	a_1	a_3	a_5
B	$0°$	$233,3 \pm 8.6$	$-36,2 \pm 11.4$	0 (fixed)
	$90°$	206.6 ± 8.8	0 (fixed)	-12.5 ± 12.9
C	$0°$	213.9 ± 7.1	-31.2 ± 9.4	0 (fixed)
	$90°$	189.9 ± 4.5	0 (fixed)	-9.1 ± 6.6

Table 5.1: Fit parameters of equation 5.19 to the experimental data in figure 5.5.

One important detail before starting the final measurement is to set the phase of the entangled state

[2] Note that fidelity is calculated with regards to one of the two $|\Psi^{target}\rangle = \frac{1}{\sqrt{2}}(|01\rangle \pm |10\rangle)$ states. Only for those two cases we observe perfect (anti)correlation in all three measurement basis. These two cases are achieved when we set the optical phase difference to be $\Delta\phi = \{0, \pi\}$. The states heralded by an event on detector 1 will be the plus state and the other detector will record the minus state. Therefore, if it is the case that we are not aiming for such optical phase difference values, instead of changing the way we calculate the fidelity, we can use a different trick - we can shift the equatorial measurement basis by $\Delta\phi$, i.e., $x' = x + \Delta\phi$ and $y' = y + \Delta\phi$. This way we can prepare an entangled state with whatever phase we want, shift the measurement basis an use the same analysis code to calculate the fidelity.

we are preparing. This can be done by preparing the same entangled state several times and measuring one NV in the x basis and the other in several different basis in the xy plane. After calculating the correlator (equation 5.16), we can plot it as a function of the phase of the measurement basis with respect to the x axis, ϕ. We expect maximum correlation when the NV's are measured in the xx basis ($\phi = 0$), no correlation for $\phi = \frac{\pi}{2}$ (node B and C being measure in x and y, respectively) and for $\phi = \pi$ maximum anti-correlation[3]. If this is not the case, then we can extract the phase of the entangled state, fitting the correlator data points to a cosine curve. The fitted phase corresponds to $\Delta\phi$. In case we intend to set a specific phase onto the entangled state, we can shift the set point W_2 by that same amount (see section 3.3).

5.2.2 Measurement

It is worth mentioning that the following data, aiming for $\Delta\phi = 0°$ was taken in two different sets. The reason for this is that this measurement would be very long and some setup parameters would significantly drift if we took the data all at once. For instance, we predict that if we would measure $\Delta\phi$ before and after the main experiment, the results wouldn't be compatible within error and we wouldn't be able to claim that $\Delta\phi$ was kept constant throughout the measurement. To avoid that, we can divide the complete experiment in steps - first we calibrate the position (see section A.1.2) and measure the tail sweep (see section A.1.14) for further calibration; then we measure the $\Delta\phi$, adjust it and measure it again to make sure we set it to the desired value; later, we take the first data set, measuring $\Delta\phi$ right after, to confirm if it stayed constant within error; we can later calibrate the position again and adjust and measure $\Delta\phi$, once again; we proceed to the second data set and a final $\Delta\phi$ measurement, right after. The optical phase difference measurements right before and after each data set are important to estimate an average $\Delta\phi$ we can associate with every data point.

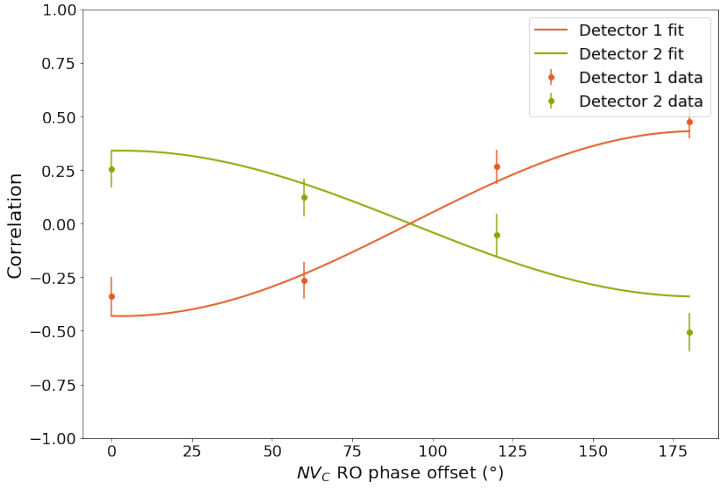

Figure 5.5: Fit of equation 4.6 with fixed $A_0 = 0$ to the experimental points of the quantum correlator (equation 5.16) as a function of the phase of the measurement basis with respect to the x axis, ϕ, for both detectors.

[3]This only applies for one of the detectors. The other one should exhibit the same behaviour although with a phase difference of π.

$\Delta\phi^{target}(^\circ)$	Data set	$\Delta\phi^{before}(^\circ)$	$\Delta\phi^{after}(^\circ)$	$\Delta\phi^{average}(^\circ)$
0	1	3.0 ± 9.7	15.0 ± 9.3	9.6 ± 5.0
	2	10.7 ± 6.5	53.4 ± 9.0	
90	1	-99.7 ± 6.3	-85.8 ± 3.1	-92.8 ± 3.5

Table 5.2: Fit parameters of equation 4.6 with fixed $F_0 = 0$ to the experimental data in figure 5.5. Note that when aiming for $\Delta\phi^{target} = 90°$, we settled for $\Delta\phi^{average} = -94°$, since for the purpose of this project, the expected behaviour should be the same for both cases. The $\Delta\phi^{average}$ obtained when aiming for $\Delta\phi = 0°$ doesn't take $\Delta\phi^{after} = 51.8°$, measured after taking the data set 2, into consideration, since it would be hard to claim that $\Delta\phi$ was approximately constant throughout that measurement. Instead, we filter out last two third of data set 2.

Proceeding to the final measurement, in figure 5.6, we plot the experimental results of the fidelity of the final entangled state with regards to the target state $\frac{1}{\sqrt{2}}(|01\rangle \pm e^{i\Delta\phi}|10\rangle)$, overlapped with the simulations developed in the previous section and based on the parameters in table 5.3 that were either pre determined - as it is the case of α, β and $\Delta\phi$ - or estimated - as it is the case of η_A and η_B that can be extracted from the optical pulse saturation calibration measurement (see section A.1.14). Relying on table 5.3, which specifies the parameters, associated with the other four sources of infidelity that were previously studied and estimated in the group, we can roughly determine the average fidelity of the prepared entangled states for a perfect excitation pulse to be $\mathcal{F}_{average}(\theta = \pi) = 0.409$. Therefore, the simulations depicted in figure 5.6 were multiplied by a factor of $\frac{0.409}{\mathcal{F}_{average}(\theta=\pi)}$ to compensate for those errors that were not taken into account in the calculations demonstrated in section 5.1.1.

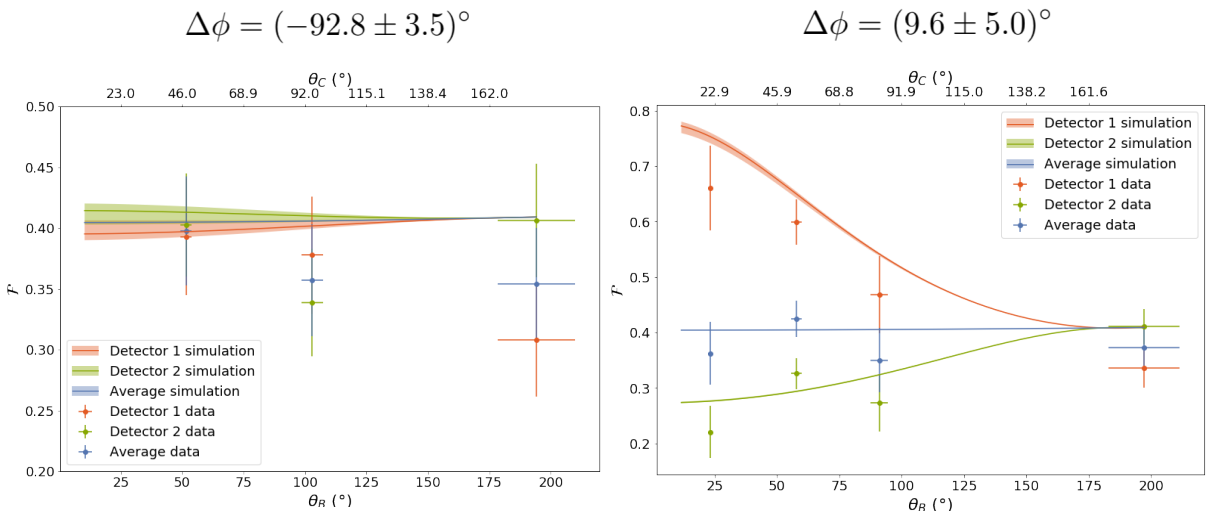

Figure 5.6: Measured fidelity of the two-node entangled state with regards to the targeted maximally entangled state as a function of the optical pulse rotation angles in nodes B (bottom axis) and C (top axis), θ_B and θ_C, respectively. The fidelity for the data points was calculated with equation 5.17, for each separate detector (red and green points), later used to calculate their average (blue points), weighted by the fraction of events recorded in each detector. The solid lines together with the same color bands correspond to the fidelity simulations according to equations 5.13 and 5.15. Both the simulations and the data points are associated with specific parameters - $\alpha_B = 0.4$, $\alpha_C = 0.6$, $\eta_B = 1.5 \times 10^4$, $\eta_C = 1.0 \times 10^4$, $\Delta\phi = -96.8°$ (left plot), $\Delta\phi = 9.6°$ (right plot). The colored bands cover the simulation values within the uncertainty associated with $\Delta\phi$. The simulations were further multiplied by a $\frac{0.409}{\mathcal{F}_{average}(\theta=\pi)}$ factor.

Analysing the $\Delta\phi = (9.6 \pm 5.0)°$ case, we observe that the simulations agree with the experimental

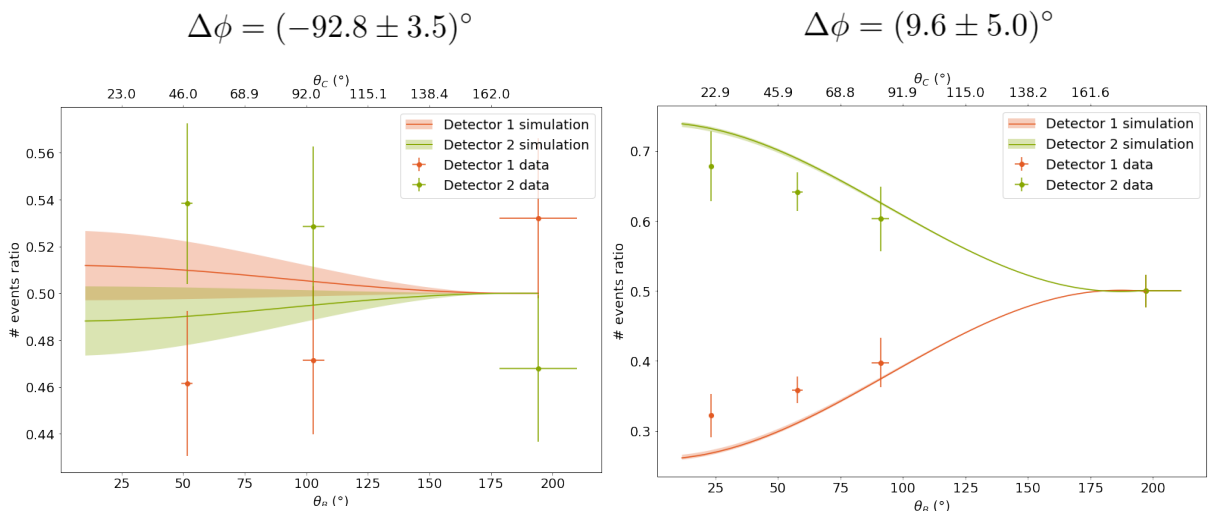

Figure 5.7: Events ratio measured by each separate detector as a function of the optical pulse rotation angles in nodes B (bottom axis) and C (top axis), θ_B and θ_C, respectively. The data points were calculated by dividing the number of events detected by each detector by the total number of photon detection events. The solid lines together with the same color bands correspond to the events ratio simulations, based on equation 5.14. Both the simulations and the data points are associated with specific parameters - $\alpha_B = 0.4$, $\alpha_C = 0.6$, $\eta_B = 1.5 \times 10^4$, $\eta_C = 1.0 \times 10^4$, $\Delta\phi = -96.8^\circ$ (left plot), $\Delta\phi = 9.6^\circ$ (right plot). The colored bands cover the simulation values within the uncertainty associated with $\Delta\phi$.

Detection window	Dark counts rate	$\|e\rangle$ lifetime	Visibility	Phase uncertainty
20×10^{-9} s	10 s^{-1}	12.1×10^{-9} s	0.7	15°

Double excitation probability	α_B	α_C	η_B	η_C
0.06	0.4	0.6	1.5×10^{-4}	1.0×10^{-4}

Table 5.3: Simulation parameters used in figures 5.6 and 5.7.

data - for $\theta = 180^\circ$ the fidelity for both detectors is the same within error bar and as θ decreases the fidelity increases for detector 1, decreases for detector 2 and the average is approximately constant. Additionally, we can verify that the fidelity can go from $\mathcal{F} \approx 0.35$ up to $\mathcal{F} \approx 0.65$, just by decreasing the probability of excitation of the optical pulse, which corresponds to the behaviour we had predicted in the previous section. For $\Delta\phi = (-92.8 \pm 3.5)^\circ$ we can also say the fidelity (for detectors 1 and 2 and their average) is approximately constant as the simulations suggest.

Finally, as another way of confirming the validity of the model described in section 5.1.1, we can also look at the fraction of events that were measured in each detector, as it is connected to the other key aspect studied in this research - the entanglement rate generation.

We observe that higher fidelity states in a particular detector come at the expense of a lower entanglement rate generation, which is more clearly seen in the $\Delta\phi = 9.6^\circ$ case (right plots in figures 5.6 and 5.7). As for $\Delta\phi = -92.8^\circ$, both detectors record approximately the same number of events, within error, as predicted in the simulations.

5.3 Interpretation of the results

We see that the fidelity's dependence on θ is itself dependent on the detector and optical phase difference $\Delta\phi$. The fidelity, for a given detector, at $\theta = \pi$ can either be maximum, minimum or equal comparing to all other θ's. Regarding the optical phase difference, $\Delta\phi$, we observe two different regimes in figures 5.3 and 5.6 - in case $\Delta\phi \approx \frac{\pi}{2}$ the fidelity (individually considered for each detector) doesn't depend on θ, whereas in case $\Delta\phi \approx 0$, the dependence on θ is different depending on which detector clicked. In order to physically understand these results, it is worth mentioning that, in this derivation, $|NV_A, NV_B\rangle = |00\rangle$ is the only state responsible for decreasing the fidelity, either because two photons were emitted and one of them was lost or both photons passed through the beam splitter and were consequently sent to the same non-number resolution detector, or because only one of the nodes was excited by the non-saturating optical pulse and therefore only one photon was emitted and detected. Consequently, only in case the photon(s) produced by such a state are disproportionately hitting one of the detectors, we can observe such a difference in fidelity, when comparing the entangled states heralded by the different detectors. Essentially, the optical phase $\Delta\phi$ sets an imbalance between the detectors or, more precisely, determines what fraction of the photons that are a product of $|NV_A, NV_B\rangle = |00\rangle$ states are sent to what detector. On the other hand, it is clear that once the imbalance is set by $\Delta\phi \approx 0$, as we move θ further away from π, this imbalance becomes larger and larger, i.e., the fidelity increases in one detector and decreases in the other. Additionally, if we look at equation 4.4, we observe that θ influences the probability of such $|00\rangle$ state being generated, therefore governing how big this imbalance can be.

5.4 Finding the most efficient entanglement generation strategy

Curiously, the simulations suggest that, if we set the right $\Delta\phi$ and choose the right detector, we should be able to achieve very high fidelity states, by decreasing the power of the optical pulse such that it is equivalent to a very small θ. Considering the initial goal was to find a pulse as close as possible to a π rotation, we now seem to be able to produce high fidelity states as further away we step from the perfect pulse. However, the measurements in section 5.2.2 suggest that these same low θ entangled states are associated with lower entanglement generation rates.

The literature [8] points to a preparation of NV's in low α superposition states as a way of achieving high fidelity states. However, tuning the right $\Delta\phi$ and θ appears as another possible way of accomplishing that same goal. The remaining question is whether we can take advantage of this effect or if it is simply equivalent to decreasing α. First, it is useful to remember the two quantities we are interested in maximizing when studying entanglement - fidelity and rate (proportional to p_{click}). Figure 5.8 illustrates the plot of both these quantities as a function of θ, considering the promising case $\Delta\phi = 0$ and $detector = 1$, to help us answer the question.

In figure 5.8, each color corresponds to a different α and is associated to a certain fidelity and probability of click, represented by the continuous and dashed lines, respectively. To more easily analyse this figure, let's say we are looking for a set of parameters corresponding to a fidelity $\mathcal{F} =$

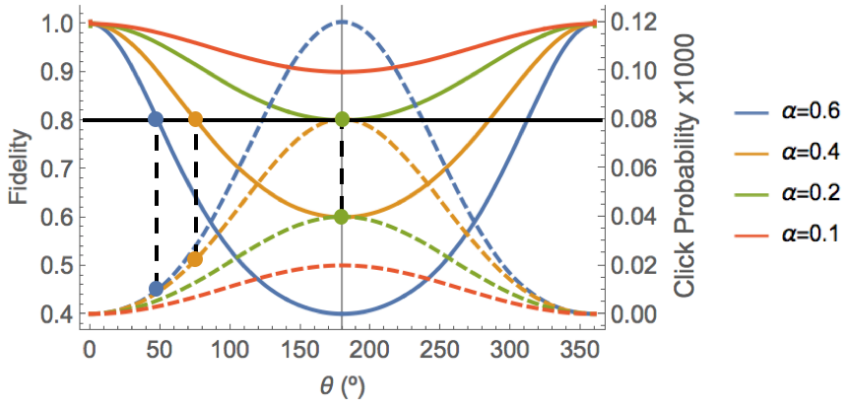

Figure 5.8: Plot of the two-node entangled state fidelity defined by equation 5.13 (solid colored lines to be read on the left side of the plot) and of the probability of click expressed in equation 5.14 (dashed colored lines to be read on the right side of the plot). The considered parameters are $\alpha = \beta$, $\theta = \theta_A = \theta_B$, $\eta_A = \eta_B = 10^{-4}$, $\Delta\phi = 0$ and $detector = 1$. The black lines and intersection points are identified for further analysis.

0.8, which can be identified by drawing an horizontal line that reads $\mathcal{F} = 0.8$ on the left side of the plot and fixing the points at which this line intersects the various continuous fidelity lines - $(\alpha, \theta) \approx \{(0.2, 180°), (0.4, 75°), (0.6, 45°)\}$. Using theses same parameters, we can compare to what probability of click these parameters lead to, by drawing a vertical line associated with each previously identified θ and finding its intersection with the associated α dashed line - $(\alpha, \theta, P_{click} \times 10^3) \approx \{(0.2, 180°, 0.04), (0.4, 75°, 0.02), (0.6, 45°, 0.01)\}$. This analysis suggests that the probability of click increases as closer we get to $\theta = 180°$. Re-framing this result in the bigger picture, although we can indeed play both with α and θ to arrive at the same fidelity, if we simultaneously want to maximize the rate at which such states are generated, then we should go back to the initial goal of calibrating the optical pulse at $\theta = \pi$.

Although the analysis of figure 5.8 is good to gain some intuition on the fidelity vs rate dynamics as a function of θ, it doesn't allow us to take definite conclusions regarding the parameters that maximize the combined fidelity and rate, since we are only looking at a discrete selection of parameters, leaving aside many other sets of possibilities. To generalize the analysis, we start by simplifying equations 5.13 and 5.14 to equations 5.20 and 5.21, respectively, by considering $\alpha = \beta$, $\theta_A = \theta_B = \theta$ and $\eta_A = \eta_B = \eta \ll 1$ (this approximation is validated by the measured experimental efficiency $\eta \approx 10^{-4}$, which is indeed much smaller than 1).

$$\begin{aligned} \mathcal{F}(\alpha, \theta, \Delta\phi) &= \frac{4\eta(\alpha - 1)}{\eta(\alpha\eta - 4) + 2\alpha\eta\cos(\Delta\phi) + \alpha(2\eta\cos(\Delta\phi) - \eta^2)\cos\theta} \overset{(\eta \ll 1)}{\approx} \\ &\approx \frac{1 - \alpha}{1 - \cos(\Delta\phi)\cos^2\frac{\theta}{2}} \end{aligned} \tag{5.20}$$

$$\begin{aligned} p_{click}(\alpha, \theta, \eta, \Delta\phi) &= \frac{1}{2}\alpha\left(4\eta + \alpha\eta^2(\cos\theta - 1) - 2\alpha\eta\cos(\Delta\phi) - 2\alpha\eta\cos(\Delta\phi)\cos\theta\right)\sin^2\frac{\theta}{2} \overset{(\eta \ll 1)}{\approx} \\ &\approx 2\alpha\eta\sin^2\frac{\theta}{2}\left(1 - \cos(\Delta\phi)\cos^2\frac{\theta}{2}\right) \end{aligned} \tag{5.21}$$

We see that while the detection efficiency, η, doesn't affect the fidelity, it proportionally changes the

probability of generating entanglement. Therefore, it is clear that we should always try to maximize η, through the calibrations (see section A) and alignment. We then proceed to find the set of parameters that, for the same fidelity:

$$\begin{aligned}
&\mathcal{F}(\alpha,\pi,\Delta\phi) = \mathcal{F}(\beta,\theta,\Delta\phi) \Leftrightarrow \\
&\Leftrightarrow 1-\alpha = \frac{1-\beta}{1-\beta\cos(\Delta\phi)\cos^2\frac{\theta}{2}} \Leftrightarrow \\
&\Leftrightarrow \sin^2\frac{\theta}{2} = \underbrace{1-\frac{1}{\beta\cos(\Delta\phi)}\left(1-\frac{1-\beta}{1-\alpha}\right)}_{f_1(\alpha,\beta,\Delta\phi)} \in]0,1],
\end{aligned} \tag{5.22}$$

results in a higher rate than the one associated with $\theta = \pi$:

$$\begin{aligned}
&p_{click}(\alpha,\pi,\eta,\Delta\phi) < p_{click}(\beta,\theta,\eta,\Delta\phi) \Leftrightarrow \\
&\Leftrightarrow 2\alpha\eta < 2\beta\eta\sin^2\frac{\theta}{2}\left(1-\beta\cos(\Delta\phi)\cos^2\frac{\theta}{2}\right) \Leftrightarrow \\
&\Leftrightarrow 0 < \underbrace{(1-\beta)\left(\beta-\frac{1}{\cos(\Delta\phi)}\left(1-\frac{1-\beta}{1-\alpha}\right)\right)}_{f_2(\alpha,\beta,\Delta\phi)}.
\end{aligned} \tag{5.23}$$

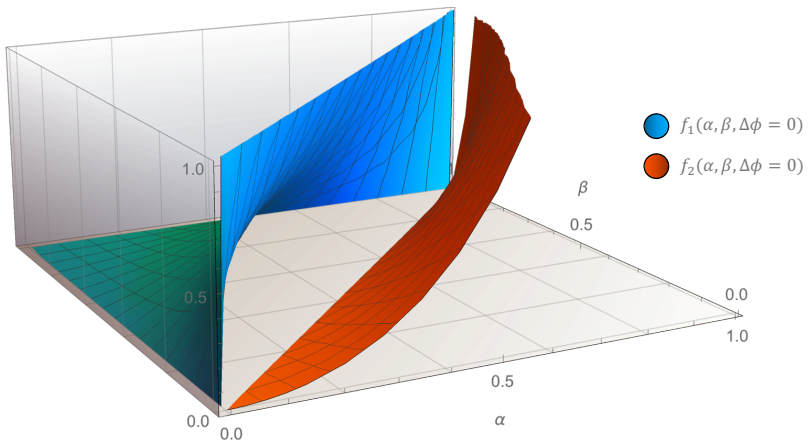

Figure 5.9: 3D plot of functions f_1 (blue) and f_2 (orange) defined in (in)equations 5.22 and 5.23, respectively, as a function of α and β and for $\Delta\phi = 0$.

We now have two conditions that need to be simultaneously verified in order to claim that we should aim for a different set of parameters than the ones initially proposed. To do that, we consider again the most promising case - $\Delta\phi = 0$ - and numerically solve both conditions in *Mathematica*. No solution was found, as visually suggested when plotting both functions f_1 and f_2 in figure 5.9.
Notice that the we are only plotting the functions in the appropriate domain of α and β, in which, both functions are never simultaneously found in the interval of interest $]0,1]$, i.e., both conditions 5.22 and 5.23 are not simultaneously verified in this domain. Therefore, we can claim that, if the setup is exclusively subject to the errors mentioned in section 5.1.1, we cannot achieve a better fidelity and rate combination than the one we get for a perfect optical π pulse.

In conclusion, in order to prepare entangled states reaching the maximum fidelity and rate combined, the calibration of the optical pulse cannot be neglected, although the fidelity and rate are less affected by fluctuations in θ, in the low α (high fidelity) regime and for values of θ close to π, where the cosine fidelity and rate curves reach an inflection point. We also see that we can use interference such that, by setting a non-perfect excitation pulse, high fidelity states are disproportionately heralded by one of the detectors. However, this comes at the cost of a lower entanglement rate.

5.4.1 Other sources of infidelity

As mentioned before, there are other sources of infidelity dismissed in this section, from which the following four were identified to be the most significant [31]:

- the optical phase difference uncertainty (see section 3.3)
- the detectors register the measurement of a photon even though they were in complete darkness, effect commonly known as dark counts
- a single optical pulse excites the NV twice, which invalidates spin-photon entangled state used to calculate the final spin-spin entangled state fidelity
- non-perfect photon indistinguishability

If all these effects occur independently, as considered in the simulations of figures 5.6 and 5.7, the fidelity could be simply corrected by a multiplying factor, not shifting the idea that the best approach to high fidelity states is through calibrating the optical pulse to be a π rotation. However this is not necessarily the case. For instance, when the optical pulse power delivered to the NV is decreased, the probability of double excitation also decreases, leading to an increase in fidelity. Therefore, it is possible that the further study of all these effects combined lead to a change of perspective.

5.5 Summary

In summary, we consistently observe the simulations and experimental data to qualitatively match. Regarding the light quantitative mismatch, it is possibly explained by a slight inaccuracy regarding the parameters estimation and by an oversimplified and faulty correction of all the extra sources of noise with a single and constant multiplying factor, since there are some indications that this method is not entirely correct, namely the expected dependence of the other sources of infidelity on θ. Nonetheless, it is clear that the general behaviour of the simulations agrees with the experimental data.

Chapter 6

Conclusion

In this work we set out to study how we could improve the fidelity of an entangled state prepared via the single click scheme. This process involved not only the simulation and experimental confirmation of the NV's electron spin state after being entangled with a photon state for different excitation pulse powers, but also the derivation and further study of its effect on the fidelity of the final two-node entangled state. In this regard, we found that the optical pulse can result in some curious interference effects.

The beginning of this investigation was prompted by the observation of oscillations, when checking the spin-photon entanglement. We experimentally confirmed that they were a direct result of non-perfect excitation of the optical pulse. In the general picture of the experiment, particularly in the high loss regime and taking into consideration the events registered by both detectors, this effect can be considered as an extra loss source just like the photon collection efficiency and all the other causes mentioned throughout this project, i.e., the (im)perfection of the excitation process, resulting from the optical pulse, won't affect the average fidelity, estimated to be $\mathcal{F} = 1 - \alpha$. Nonetheless, in the right regime, it can be the cause for the generation of high fidelity states for, what at first sight seemed to be faulty but turned out to be, more objectively, simple low excitation (small θ) optical pulses. This behaviour was simulated and experimentally confirmed with the help of the fragmented phase stabilization scheme. However, the simulations seem to suggest that in order to achieve such high fidelity states, we would need to accept a smaller entanglement generation rate, meaning that it doesn't seem to be the most efficient way of getting to the desired fidelity.

In summary, this project seems to suggest the most efficient way of generating entanglement is by finding the perfect optical π pulse, which can be done via the optical pulse saturation calibration without significantly affecting the fidelity and rate.

6.1 Future work

A complete study of the entanglement fidelity and rate, considering the non-perfect excitation of the optical pulse, dark counts, double excitation, distinguishability of the interfering photons and phase uncertainty, might lead to a different conclusion, i.e., it is possible that the high fidelity states, achieved via

low θ optical pulses, actually make the entanglement process more efficient. This is only possible if we see that the other sources of infidelity decrease in this regime, increasing the fidelity with regards to the simulations presented in section 5.1, with no damage to the rate. It is important to carry out this investigation, since it might reveal a way of boosting the fidelity of entangled states, generally contributing to the reliability of a quantum network based on NV centers.

Bibliography

[1] C. H. Bennett and G. Brassard. Quantum cryptography: Public key distribution and coin tossing. *Theoretical Computer Science*, 560:7–11, 2014. doi: 10.1016/j.tcs.2014.05.025. URL www.elsevier.com/locate/tcs.

[2] S. Wehner, D. Elkouss, and R. Hanson. Quantum internet: A vision for the road ahead, 10 2018. ISSN 10959203. URL https://science.sciencemag.org/content/362/6412/eaam9288.

[3] J. L. Park. The concept of transition in quantum mechanics. *Foundations of Physics*, 1:23–33, 3 1970. ISSN 00159018. doi: 10.1007/BF00708652. URL https://link.springer.com/article/10.1007/BF00708652.

[4] N. Gisin, G. Ribordy, W. Tittel, and H. Zbinden. Quantum cryptography. *Rev. Mod. Phys.*, 74: 145–195, 3 2002. doi: 10.1103/RevModPhys.74.145. URL https://link.aps.org/doi/10.1103/RevModPhys.74.145.

[5] L. Robledo, L. Childress, H. Bernien, et al. High-fidelity projective read-out of a solid-state spin quantum register. *Nature*, 477:574–578, 9 2011. ISSN 00280836. doi: 10.1038/nature10401. URL https://www.nature.com/articles/nature10401.

[6] N. Bar-Gill, L. M. Pham, A. Jarmola, D. Budker, and R. L. Walsworth. Solid-state electronic spin coherence time approaching one second. *Nature Communications*, 4:1–6, 4 2013. ISSN 20411723. doi: 10.1038/ncomms2771. URL https://rdcu.be/cejIF.

[7] T. H. Taminiau, J. J. T. Wagenaar, T. van der Sar, et al. Detection and control of individual nuclear spins using a weakly coupled electron spin. *Phys. Rev. Lett.*, 109:137602, 9 2012. doi: 10.1103/PhysRevLett.109.137602. URL https://link.aps.org/doi/10.1103/PhysRevLett.109.137602.

[8] P. C. Humphreys, N. Kalb, J. P. Morits, et al. Deterministic delivery of remote entanglement on a quantum network. *Nature*, 558:268–273, 6 2018. doi: 10.1038/s41586-018-0200-5. URL https://rdcu.be/cejJB.

[9] B. Hensen, H. Bernien, A. E. Dreaú, et al. Loophole-free Bell inequality violation using electron spins separated by 1.3 kilometres. *Nature*, 526:682–686, 10 2015. doi: 10.1038/nature15759. URL https://rdcu.be/cejJY.

[10] N. Kalb, A. A. Reiserer, P. C. Humphreys, et al. Entanglement distillation between solid-state quantum network nodes. *Science*, 356:928–932, 6 2017. ISSN 10959203. doi: 10.1126/science.aan0070. URL https://science.sciencemag.org/content/356/6341/928.abstract.

[11] M. A. Nielsen and I. L. Chuang. *Quantum Computation and Quantum Information*. Cambridge University Press, 2020. URL shorturl.at/hvy34.

[12] D. D. Awschalom, R. Hanson, J. Wrachtrup, and B. B. Zhou. Quantum technologies with optically interfaced solid-state spins. *Nature Photonics*, 12:516–527, 9 2018. ISSN 17494893. doi: 10.1038/s41566-018-0232-2. URL https://www.nature.com/articles/s41566-018-0232-2.

[13] F. Jelezko and J. Wrachtrup. Single defect centres in diamond: A review, 10 2006. URL https://doi.org/10.1002/pssa.200671403.

[14] H. Bernien. *Control, measurement and entanglement of remote quantum spin registers in diamond*. PhD thesis, Technical University of Delft, 2 2014. URL https://doi.org/10.4233/uuid:75130c37-edb5-4a34-ac2f-c156d377ca55.

[15] M. W. Doherty, N. B. Manson, P. Delaney, et al. The nitrogen-vacancy colour centre in diamond. *Physics Reports*, 528:1 – 45, 2013. ISSN 0370-1573. doi: https://doi.org/10.1016/j.physrep.2013.02.001. URL http://www.sciencedirect.com/science/article/pii/S0370157313000562.

[16] M. L. Bellac and P. de Forcrand-Millard. *A short introduction to quantum information and quantum computation*. Cambridge University Press, 1 2006. doi: 10.1017/CBO9780511755361. URL https://doi.org/10.1017/CBO9780511755361.

[17] C. Cabrillo, J. I. Cirac, P. García-Fernández, and P. Zoller. Creation of entangled states of distant atoms by interference. *Phys. Rev. A*, 59:1025–1033, 2 1999. doi: 10.1103/PhysRevA.59.1025. URL https://link.aps.org/doi/10.1103/PhysRevA.59.1025.

[18] L. M. Duan, M. D. Lukin, J. I. Cirac, and P. Zoller. Long-distance quantum communication with atomic ensembles and linear optics. *Nature*, 414:413–418, 11 2001. ISSN 00280836. doi: 10.1038/35106500. URL https://rdcu.be/cejI8.

[19] D. L. Moehring, P. Maunz, S. Olmschenk, et al. Entanglement of single-atom quantum bits at a distance. *Nature*, 449:68–71, 9 2007. doi: 10.1038/nature06118. URL https://rdcu.be/cejJl.

[20] P. C. Maurer, G. Kucsko, C. Latta, et al. Room-temperature quantum bit memory exceeding one second. *Science*, 336:1283–1286, 6 2012. doi: 10.1126/science.1220513. URL https://science.sciencemag.org/content/336/6086/1283.

[21] L. M. K. Vandersypen and I. L. Chuang. Nmr techniques for quantum control and computation. *Rev. Mod. Phys.*, 76:1037–1069, 1 2005. doi: 10.1103/RevModPhys.76.1037. URL https://link.aps.org/doi/10.1103/RevModPhys.76.1037.

[22] M. V. Gurudev Dutt, L. Childress, L. Jiang, et al. Quantum register based on individual electronic and nuclear spin qubits in diamond. *Science*, 316:1312–1316, 6 2007. doi: 10.1126/science.1139831. URL https://science.sciencemag.org/content/316/5829/1312.

[23] G. D. Fuchs, G. Burkard, P. V. Klimov, and D. D. Awschalom. A quantum memory intrinsic to single nitrogen-vacancy centres in diamond. *Nature Physics*, 7:789–793, 10 2011. ISSN 17452473. doi: 10.1038/nphys2026. URL https://www.nature.com/articles/nphys2026.

[24] F. Rozpedek, R. Yehia, K. Goodenough, et al. Near-term quantum-repeater experiments with nitrogen-vacancy centers: Overcoming the limitations of direct transmission. *Phys. Rev. A*, 99:052330, 5 2019. doi: 10.1103/PhysRevA.99.052330. URL https://link.aps.org/doi/10.1103/PhysRevA.99.052330.

[25] Z.-H. Wang, G. de Lange, D. Ristè, R. Hanson, and V. V. Dobrovitski. Comparison of dynamical decoupling protocols for a nitrogen-vacancy center in diamond. *Phys. Rev. B*, 85:155204, 4 2012. doi: 10.1103/PhysRevB.85.155204. URL https://link.aps.org/doi/10.1103/PhysRevB.85.155204.

[26] One-second coherence for a single electron spin coupled to a multi-qubit nuclear-spin environment. *Nature Communications*, 9:1–8, 12 2018. ISSN 20411723. doi: 10.1038/s41467-018-04916-z. URL https://rdcu.be/cejJ0.

[27] C. E. Bradley, J. Randall, M. H. Abobeih, et al. A ten-qubit solid-state spin register with quantum memory up to one minute. *Phys. Rev. X*, 9:031045, 9 2019. doi: 10.1103/PhysRevX.9.031045. URL https://link.aps.org/doi/10.1103/PhysRevX.9.031045.

[28] W. Pfaff. *Quantum measurement and entanglement of spin quantum bits in diamond*. PhD thesis, Technical University of Delft, 10 2012. URL https://doi.org/10.4233/uuid:62208a4a-72c6-45b5-af51-1a8e8f8bfdd8.

[29] K. K. Sharma. *Optics, principles and applications*. Academic Press, 2006.

[30] S. Hermans. Phase stabilization for three node experiments, 2020.

[31] N. Kalb. *Diamond-based quantum networks with multi-qubit nodes*. PhD thesis, TU Delft, 4 2018. URL https://doi.org/10.4233/uuid:249753ae-9000-446a-9375-63c1e1165cc1.

[32] *Introductory Quantum Optics*. Cambridge University Press, 10 2004. ISBN 9780521527354. doi: 10.1017/CBO9780511791239. URL https://www.cambridge.org/core/product/identifier/9780511791239/type/book.

[33] H. Beukers. Improving coherence of quantum memory during entanglement creation between nitrogen vacancy centres in diamond. Master's thesis, TU Delft, 2 2019. URL http://fse.studenttheses.ub.rug.nl/id/eprint/19196.

Appendix A

Calibration Routine

The three available set ups need to be calibrated so that the experiments can be successfully executed and the analysis and conclusions can be reliable. Depending on the nature of the experiment, different calibrations are required. Given that the aim of this project involves generating remote entanglement between the nodes, the single setup calibrations need to be followed by multi-setup calibrations.

A.1 Single-setup

A.1.1 Calibrate the lasers

We want to be able to select the power we want from each laser. For that we need to know the correspondence between the output power and the amplitude of oscillating electric signal applied to the AOM, via the ADWIN and/or AWG.

A.1.2 Optimize on position:

There is a microscope objective located inside the cryostat that focuses light onto the sample and collects the emission photons. Therefore, in order to maximize the efficiency of the experiments, we need to optimize the position of the NV relative to the objective. This is achieved by sending green light and setting the sample (or objective, depending on the setup) in a position such that the number of collected photons is maximized.

A.1.3 Getting the lasers on resonance

We need to ensure that the lasers are well on resonance with the optical transitions we want to address. The way we do this is by running a set of CR checks (that turns on both red lasers) and tuning the lasers to the frequencies that lead to the larger number of counts per CR check.

A.1.4 Check ZPL alignment

Since the ZPL photons are just a small fraction of the light emitted by the NV, we need to make sure we maximize its detection efficiency. Consequently, it is critical to improve the coupling of the ZPL photons to the single-mode optical fibers that lead them to the detectors. To optimize that coupling, the setup incorporates a deformable mirror that we can reshape. For that, we turn on the green light to excite the NV, sweep different Zernike modes and find the optimum shape that will correspond to a linear combination of the different modes, such that the detection of ZPL photons is maximized.

A.1.5 Single shot read out

Before any other qubit control calibration, it is necessary to determine the read out pulse duration that leads to a larger fidelity. Additionally, we need to be able to quantitatively characterize the read out method, so that its error can be propagated and taken into account in the final results of any experiment. Therefore, we initialize the electron spin, read out its state and repeat the same sequence for a range of different read out durations. This calibration is performed for both $m_s = 0$ and $m_s = \pm 1$ initial states. In principle, for the initialization in the $m_s = 0$ state, the larger the RO time, the larger the probability of detecting a photon and, consequently, the larger the fidelity. However, the measurement of the $m_s = \pm 1$ state consists of not detecting any photon, which means that the larger the RO time, the smaller the fidelity. Therefore, the single-shot read out calibration sets the RO duration that corresponds to the largest average fidelity.

A.1.6 Dark ESR (electron spin resonance)

It is important that the NV ground-state transition frequencies are known, in order to properly control the qubit state transitions $|0\rangle \leftrightarrow |1\rangle$. This calibration starts with an initialization of the electron spin in the $|0\rangle$ state, followed by the application of a MW pulse, and finally, the read out of the electron spin state. We repeat the same sequence and sweep of the frequency of the MW pulse. It is expected that, once the frequency of the MW matches the ground-state transition frequencies of the electron spin, the probability of measuring the $|0\rangle$ state decreases. Additionally, considering the NV ground-state transitions dependence on the nitrogen-state, three close frequencies should be identified for all spin state transition, each one corresponding to a different nitrogen state.

A.1.7 MW π rotation

As mentioned in section 2.2.2, a MW can be used to control the electron spin state, i.e., to perform arbitrary rotations. The angle of these rotations is determined by the amplitude and the duration of the MW pulse. For this experiment, the pulse needs to cover all three transition frequencies found in the dark esr calibration, which means that the MW pulse needs to be short. Therefore, in order to calibrate a full π rotation, able to flip the $|0\rangle$ state to the $|1\rangle$ state and vice-versa, we can sweep the MW pulse

amplitude and read out the electron spin such that we are able to find the point where the electron spin is completely flipped.

A.1.8 Skewness

As mentioned in section 2.2.2, the MW pulse frequency is determined by the transition frequency of the $m_s = 0$ and $m_s = \pm 1$ two-level system. However, the MW pulse frequencies are transmitted depending on the transfer function of each setup, which means some frequencies in the Hermite MW pulse range are more efficiently transmitted than others and consequently, the shape of the pulse is deformed. In order to correct this distortion and maximize the fidelity of a MW pulse, the Fourier transform of the Hermite pulse is multiplied by a linear function [33]. More specifically, the calibration consists on applying π pulses and sweeping the slope of this linear function (that we call skewness of the pulse), such that we determine the value that gets us closer to the $|1\rangle$ state.

A.1.9 Single shot read out with MW initialization

The same principle as for the first single shot read out calibration applies but, in this case, the electron spin is initialized using the MW pulse calibrated in the MW π calibration, since it is the initialization method that is used in the experiments. Therefore, a new optimum MW pulse duration is determined and set in the parameters.

A.1.10 MW $\frac{\pi}{2}$ rotation

This calibration takes into account that a $\frac{\pi}{2}$ and $\pi - \frac{\pi}{2}$ rotations around the same axis should be equivalent. Therefore, the MW amplitude is swept such that we find the value for which, for both situations, the final state is in the x axis, using the same MW amplitude and MW pulse duration parameters.

A.1.11 Theta rotation

The same principle as for the MW π calibration applies but in a more general way, i.e., instead of calibrating a single transition ($|0\rangle \leftrightarrow |1\rangle$), it calibrates the MW pulse for a range of different superposition states. The calibration range is restricted to what is considered to be useful for the experiment, such that the control of the electron spin state is more reliable.

Multi-setup calibration

Optimize rejection of the reflected light

Some of the light that is sent to the NV to spin pump or read out the electron spin can be reflected back, going though the same path of the ZPL photons. This can turn into a problem because we might be mistaking laser light for ZPL photons. However, if we use a waveplate to set the polarization of

the excitation light to be almost orthogonal to the polarization of the electron spin, we will be able to further filter the reflected light from the ZPL photons, with the help of extra waveplates and a polarizer. Therefore, we can turn on the laser, set its polarization with the cryo half wave plate (see section 3.2) and finally, rotate a half-wave plate and a quarter-wave plate, such that we minimize the light going though the polarizer to the detector.

A.1.12 Optical pulse - EOM and AOM

The entanglement generation rate and fidelity highly depend on the calibration of the optical pulse, responsible for the excitation of NV's. As mentioned in section 3.2, this laser light goes through an AOM and an EOM for pulse modulation. The shape of the final pulse will depend on the voltage applied to the EOM and on the amplitude of the oscillating electrical signal applied to the AOM, which means that both settings need to be calibrated.

The on voltage that needs to be applied to the EOM is already determined by the fabricator. However, it is important to calibrate the EOM off voltage, i.e., the voltage for which the pulse coming out the EOM reaches the lowest power possible. For that, we send optical light pulses for a range of off voltages applied to the EOM and record the tail counts[1] per shot.

Finally, in order to ensure that the pulse is able to fully excite the electron spin, we send pulse light shots to the NV, for a range of different AOM amplitudes[2], record the tail counts per shot and check the amplitude for which the tail counts reach a plateau.

A.1.13 Check the phase light

In the global phase stabilization measurement (see section 3.3) it is necessary that we know the intensity of the input light such that, by measuring the output light, we can determine the optical phase difference, $\Delta\phi$. Therefore, we can turn on the phase light laser (purple solid lines in figure 3.3), block the light from one of the setups such that we can measure the light intensity from each arm of the interferometer at a time, and rotate a half wave plate, placed between the laser and the central beam splitter, until we measure the desired intensity in the single photon detectors.

A.1.14 Optical pulse saturation calibration

This calibration step fits the purpose of finding the optical pulse power that completely excites the NV. This is achieved first by preparing the NV in the $|+\rangle$ superposition state and then applying an optical pulse with varying powers (more specifically changing the AOM amplitude) and measuring the number of detected photons. As we increase the power we should see an increse in the number of photons until the point where it saturates (reaches the perfect π rotation). We estimated that for a perfect π pulse we should record an average of 0.12 counts. If this requirement is met for a specific power, then we set the aom amplitude of the optical pulse to that same value.

[1] Tail counts refer to the number of photons considered to be emitted during decay, after an optical excitation pulse.

[2] AOM amplitude refers to the amplitude of the signal sent to the RF source that will then output an oscillating electrical signal to the AOM.

Appendix B

Corrections and Errors

As in any experimental project, the experimental results presented in this project have errors associated. This appendix aims to clarify how they were calculated.

All the errors are propagated as:

$$\sigma_{f(x,y,z,...)} = \sqrt{\left(\frac{\partial f}{\partial x}\right)^2 \sigma_x^2 + \left(\frac{\partial f}{\partial y}\right)^2 \sigma_y^2 + \left(\frac{\partial f}{\partial z}\right)^2 \sigma_z^2 + \ ...} \tag{B.1}$$

B.0.1 SSRO correction

This correction is applied to every NV electron spin state measurement presented in this work. In the single shot read out calibration (see section A.1.5), we can determine the fidelity, F_0 and F_1, associated with each state, $|0\rangle$ and $|1\rangle$, respectively, by calculating the fraction of times that the qubit prepared in $|i\rangle$ is measured to be in that same state. Relying on these two quantities, we can build an operator

$$\hat{R} = \begin{pmatrix} F_0 & 1-F_1 \\ 1-F_0 & F_1 \end{pmatrix}, \tag{B.2}$$

that relates the measured populations, $\mathbf{M} = (m_0, m_1)^T$, with the expected populations, $\mathbf{P} = (p_0, p_1)^T$, as:

$$\mathbf{M} = \hat{R}\,\mathbf{P}. \tag{B.3}$$

This equation assumes that the measured population in a certain state is equal to the correctly assigned population in that state plus the incorrectly assigned population in the other state.

The SSRO correction aims to obtain the expected populations **P**, by correcting every qubit's state measurement, experimentally obtained as:

$$\begin{matrix} m_0 = \dfrac{N_0}{N} \\ m_1 = 1 - m_0 \end{matrix}, \tag{B.4}$$

where N_i is the number of times we measured the $|i\rangle$ state out of the total number of repetitions of that

same experiment, N, with the help of the $\hat{R}$ operator, experimentally obtained with the SSRO calibration. Finally, we simply need to invert equation B.3, arriving at:

$$\mathbf{P} = \hat{R}^{-1}\,\mathbf{M}, \tag{B.5}$$

or more specifically:

$$\begin{aligned} p_0 &= \frac{F_1 m_0 + (F_1 - 1)m_1}{F0 + F_1 - 1} \\ p_1 &= \frac{(F_0 - 1)m_0 + F_1 m_1}{F_0 + F_1 - 1} \end{aligned}. \tag{B.6}$$

Uncertainty

The probability distribution of N_0 is the Binomial distribution, whose variance is $Nm_0(1-m_0)$. Therefore, we can calculate the uncertainty of m_0 as:

$$\sigma_{m_0} = \sigma_{m_1} = \sqrt{\frac{m_0(1-m_0)}{N}}, \tag{B.7}$$

propagating to the expected populations uncertainty:

$$\sigma_{p_0} = \sigma_{p_1} = \frac{\sigma_{m_0}}{F_0 + F_1 - 1}. \tag{B.8}$$

Appendix C

Supplementary Figures

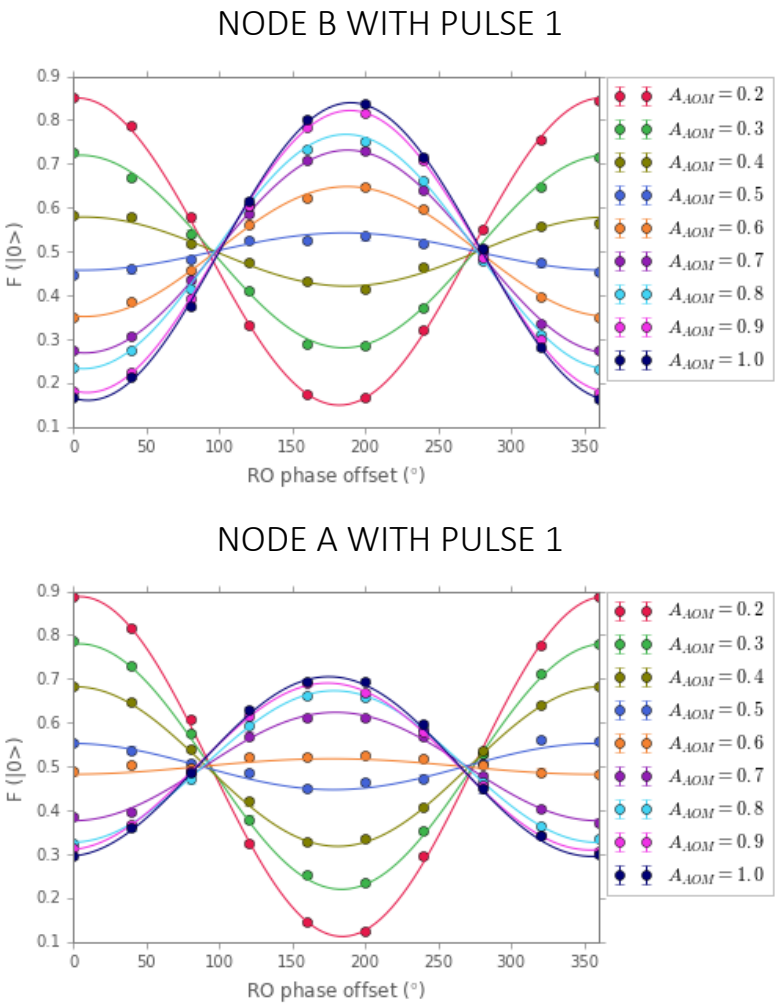

Figure C.1: Fit of the function 4.6 to the experimental points after applying the sequence in figure 4.1 with $\alpha = 0.5$. The y axis of the plot corresponds to the fidelity of the NV's electron spin state with the $|0\rangle$ state, after a rotation to the right read out basis, while the x axis corresponds to the read out phase in the xy of the Bloch sphere. The 0 degrees RO phase corresponds to the positive x axis. The different colors correspond to different AOM amplitudes that are related to power of the optical pulse.

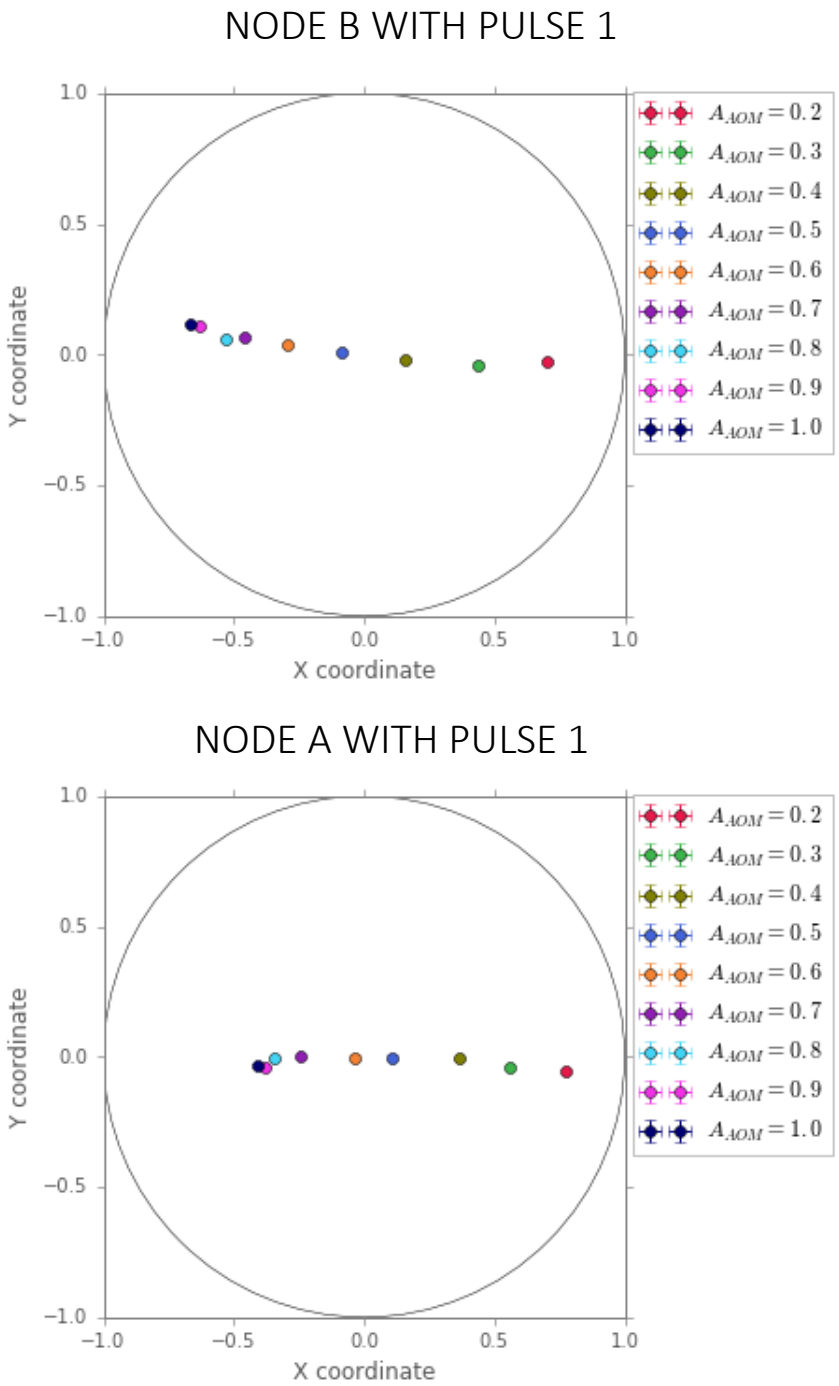

Figure C.2: Top view Bloch sphere representation of the measured NV's electron spin state vector x and y coordinates after applying the sequence in figure 4.1 with $\alpha = 0.5$.